ESA contract
Martian Environmental Model

Ref : ESA 11369/95/NL/JG(SC)

WPII deliverable :

Detailed Design Document for the Martian Atmospheric General Circulation Model

Richard Fournier, Franois Forget, Matthew Collins and Frdric Hourdin
LMD/AOPP

Approved by Olivier Talagrand May 30, 2008

Final

Abstract

This documents presents the physics and numerics for the parts of the LMD/AOPP Martian Atmospheric General Circulation Model which have been developed in the frame of the ESA contract.

The new parametrisations are: 1) a sophisticated model of the planetary boundary layer with prediction of the statistics of small scale turbulent dynamical fields, 2) a very elaborated representation of the effect of orography on the large scale flow, 3) a parametrisation of the radiative effect of condensing CO_2, and 4), an improvement of the radiative transfer code with an accurate representation of infrared scattering and a new set of parameters for dust radiative properties.

Detailed Design Document for the Martian Atmospheric General Circulation Model

Richard Fournier, Franois Forget, Matthew Collins and Frdric Hourdin

May 30, 2008

Contents

1 introduction

The complete LMD/AOPP Martian Atmospheric General Circulation Model has already been intensively described in publications (Hourdin, 1992; Hourdin et al., 1993, 1995) and will be documented in details in a document which will be delivered together with the user manual at the end of the contract (a draft version is already available).

The aim of the present document is to describe specifically the parametrisations which have been either developed or improved in the frame of the ESA contract.

Those new parametrizations are: 1) a sophisticated model of the planetary boundary layer with prediction of the statistics of small scale turbulent dynamical fields, 2) a very elaborated representation of the effect of orography on the large scale flow, 3) a parametrisation of the radiative effect of condensing CO_2, and 4), an improvement of the radiative transfer code with an accurate representation of infrared scattering and a new set of parameters for dust radiative properties.

For each parametrisation, we give a description of the physics and of the numerics involved in the parametrisation (especially when it is a crucial point as for the planetary boundary layer scheme) and we provide a well documented interface of all the corresponding subroutines.

The tests and validations of the various subroutines are presented in an independent document.

2 New turbulent diffusion scheme design

2.1 Introduction

LMD and AOPP models of Martian atmospheric circulation include a model of Martian planetary boundary layer that was designed to meet the following requirements :

i) accurate representation of surface drag effects on general circulation ;

ii) realistic modeling of near surface wind and temperature conditions.

This model includes a parametrisation of turbulent diffusion based on a model for representation of temporal evolutions of turbulent kinetic energy. The knowledge of local turbulent kinetic energy allows to predict temperature and wind standard deviations, which is of primary importance for analysis of low atmosphere conditions (entry profiles simulations, surface conditions simulations).

The present document includes :

i) description of the turbulent kinetic energy evolution equation (Sec. 2.2) ;

ii) description of the assumptions underlying the parametrisation scheme (Sec. 2.3) ;

iii) description of the algorithm (Sec. 2.4).

2.2 Temporal evolution of turbulent kinetic energy

Mellor and Yamada (1982) (see also Helfand and Labraga, 1988) have proposed a set of models of turbulent kinetic energy evolution in planetary boundary layers. The most commonly used as good compromise between accuracy and computational requirements is named the Mellor and Yamada 2.5 model : this model is a second order closure model that accounts for turbulent thermoconvection in stratified stable or unstable conditions.

The following notations are used. q is a representation of the wind standard deviation associated to turbulent fluctuations. $E = \frac{q^2}{2}$ is the turbulent kinetic

energy. l is a length scale representative of large scale structures ; it is called the master length scale. M is the mean shear :

$$M = \sqrt{\left(\frac{\partial u}{\partial z}\right)^2 + \left(\frac{\partial v}{\partial z}\right)^2} \tag{1}$$

G_M and G_H are the dimensionless square of the mean shear and the negative of the dimensionless square of the Brunt-Vaisala frequency :

$$G_M = \frac{l^2}{q^2} M^2 \tag{2}$$

and

$$G_H = -\frac{l^2}{q^2} \frac{g}{\theta_0} \frac{\partial \theta}{\partial z} \tag{3}$$

where u and v are the components of horizontal velocity, θ is the potential temperature and θ_0^{-1} is the coefficient of thermal expansion. Two stability functions S_M and S_H are also introduced in the original Mellor and Yamada 2.5 scheme that are direct functions of G_M and G_H. However Galperin et al. (1988) have proposed new expressions that are functions of G_H only :

$$S_M = \frac{0.393 - 3.09 G_H}{1 - 40.8 G_H + 212 G_H^2} \tag{4}$$

and

$$S_H = \frac{0.494}{1 - 34.7 G_H} \tag{5}$$

These stability functions have been tuned experimentally so that turbulent diffusion coefficients for velocity and potential temperature are respectively :

$$K_M = q l S_M \tag{6}$$

and

$$K_H = q l S_H \tag{7}$$

When assuming that the vertical diffusion of turbulent kinetic energy is negligible compared to local sources and sinks, the temporal evolution of turbulent kinetic energy may be written :

$$\frac{l}{q^3} \frac{\partial E}{\partial t} = S_M G_M + S_H G_H - \frac{1}{B_1} \tag{8}$$

where B_1 is a constant of proportionality taken as $B_1 = 15.0$. This set of equations is closed when specifying the master length scale. We retained Blackadar's formula (Blackadar, 1962) with $l_0 = 160m$:

$$l = \frac{\kappa z}{1 + \frac{\kappa z}{l_0}} \tag{9}$$

where κ is von Karmans constant.

This model is an excellent solution for turbulent diffusion representation ; it is however numerically very sensitive and requires both fine temporal and spatial discretisations. Its direct use for GCM simulations is therefor excluded. We implemented it in a one dimensional atmospheric column model to produce reference solutions for planetary boundary layer profiles (see Technical note on the GCM testing) and designed a new efficient parametrisation scheme adapted to Martian conditions.

2.3 Coupled stationary solution

A first solution could be the use of Mellor and Yamada 2.0 model in which it is assumed that the turbulent kinetic energy takes its stationary solution (Helfand and Labraga, 1988). Tests in strongly stratified configurations indicated that this assumption is not realistic. Despite the fact that time constantes of Eq. 8 are very small, the stationary solution is meaningless because of the strong coupling with the wind profile. The assumption that time constants of turbulence establishment are very small compared to GCM time steps is valid but this establishment is a process that is strongly coupled to local wind shear evolution. This means that M (that appears through G_M in the right side of Eq. 8) is a function of q that cannot be assumed constant when looking at stationary solutions of the turbulent kinetic energy.

On the one hand, M is not a direct function of q and the stationary solution of Eq. 8 coupled with wind shear evolution cannot be found simply. On the other hand, time constants of Eq. 8 are so small that its unstationary resolution requires small time steps incompatible with GCM requirements.

The proposed scheme assumes a simplified evolution law for M as a function of time and q : $M = M(q,t)$. This allows the stationary resolution of Eq. 8 in a way that accounts for responses of local wind shear to turbulent kinetic energy variations. For this purpose, we assume that the coordinate system is oriented in such a way that $v = 0$ (which allows to write $M = \frac{\partial u}{\partial z}$) and we write that the horizontal wind tendency due to turbulent diffusion is :

$$\left(\frac{\partial u}{\partial t}\right)_{diff} = \frac{\partial}{\partial z}\left(K_M \frac{\partial u}{\partial z}\right) = \frac{\partial}{\partial z}\left(K_M M\right) \tag{10}$$

Consequently, the wind shear tendency due to turbulent diffusion is :

$$\left(\frac{\partial M}{\partial t}\right)_{diff} = \frac{\partial^2}{\partial z^2}\left(K_M M\right) \tag{11}$$

and we observed that q could be estimated as the coupled stationary solution of Eq. 8 and Eq. 11 :

$$S_M G_M + S_H G_H - \frac{1}{B_1} = 0 \tag{12}$$

and

$$\frac{\partial^2}{\partial z^2}\left(K_M M\right) = 0 \tag{13}$$

2.4 Numerical algorithm

The system of equations (Eq. 12,Eq. 13) has two unknowns q and M. All other quantities are assumed constant. Eq. 13 is discretised and when computing q_i and M_i at the i-th atmospheric layer interface, the assumption is made that q_{i-1}, M_{i-1}, q_{i+1} and M_{i+1} are constants. Eq. 13 can therefore be written as

$$K_{M,i} M_i = F \tag{14}$$

where F is a constant wind flux :

$$F = \frac{\frac{1}{dz_i} K_{M,i+1} M_{i+1} + \frac{1}{dz_{i-1}} K_{M,i-1} M_{i-1}}{\frac{1}{dz_i} + \frac{1}{dz_{i-1}}} \tag{15}$$

dz_{i-1} and dz_i are the thicknesses of the (i-1)-th and i-th atmospheric layers. With this simplification, the system can be solved locally for each atmospheric layer.

The system could be solved numerically as such by use of an iteration process. However, this could be the source of numerical difficulties and considering the range of very distinct configurations that are to be encountered in GCM simulations, we preferred a simplified algorithm. This algorithm is strictly valid in the limit case of strongly stratified atmospheres and proved accurate enough for most configurations.

The simplified algorithm is described hereafter with the convention that all variable indexed 0 are variables at time t and all non indexed variables are unknowns a time $t + dt$:

i) M is computed as the solution of Eq. 12 under the assumptions that $S_M G_M$ and $S_H G_H$ are independent of q :

$$S_{M,0} G_{M,0} \frac{M^2}{M_0^2} + S_{H,0} G_{H,0} - \frac{1}{B_1} = 0 \tag{16}$$

ii) q is computed from the knowledge of M with Eq. 14 under the assumption that $S_M G_M$ is proportional to q^2 :

$$\frac{S_{M,0}}{q_0^2} q^3 l M = F \tag{17}$$

This algorithm requires no iteration and is very robust. It is strictly valid in the limit case of strongly stratified atmospheres which is typical of Martian night conditions. It is indeed easy to observe that $S_M G_M$, $S_H G_H$ and $\frac{S_H}{q^2}$ are asymptotic functions of q :

$$\lim_{q \to 0} S_M G_M = \frac{3.09}{212.} \frac{M^2}{\frac{g}{\theta_0} \frac{\partial \theta}{\partial z}} \tag{18}$$

$$\lim_{q \to 0} S_H G_H = -\frac{0.494}{34.7} \tag{19}$$

and

$$\lim_{q \to 0} \frac{S_H}{q^2} = \frac{0.494}{34.7} \frac{1}{l^2 \frac{g}{\theta_0} \frac{\partial \theta}{\partial z}} \tag{20}$$

Although the simplified algorithm is not valid for non strongly stratified configurations, it appeared to give reasonable results under the assumption $\frac{\partial \theta}{\partial z} = 0$ that can be made for most Martian day conditions when convective adjustment mixes the atmosphere until uniform potential temperatures. This assumptions leads to $G_H = 0$ and therefore S_M is constant : $S_M = 0.393$. Eq. 12 becomes

$$B_1 S_M l^2 M^2 = q^2 \tag{21}$$

which can be reported in Eq. 14 to give :

$$q^2 = \sqrt{\frac{B_1}{S_M}} F \tag{22}$$

It can be noted that the simplified algorithm leads to a similar solution under the same assumptions. Eq. 16 gives :

$$M^2 = \frac{q_0^2}{S_M l^2 B_1} \tag{23}$$

and Eq. 17 leads to :

$$\frac{q^3}{q_0} = \sqrt{\frac{B_1}{S_M}} F \tag{24}$$

which is comparable to Eq. 22 provided that the conditions do not vary to much from one time step to the other.

2.5 Computational aspects

The major change in terms of computational aspects is the replacement of the routine vdif_k.f with the new routine vdif_kshera.f that computes the evolution of turbulent kinetic energy and turbulent diffusion coefficients :

```
      SUBROUTINE vdif_kshear(dt,g,zlev,zlay,u,v,theta,cd,q2,km,kn)
      IMPLICIT NONE
c.....................................................................
c
c dt : pas de temps
c g  : g
c zlev : altitude a chaque niveau (interface inferieure de la couche
c        de meme indices)
c zlay : altitude au centre de chaque couche
c u,v : vitesse au centre de chaque couche
c       (en entree : la valeur au debut du pas de temps)
c theta : temperature potentielle au centre de chaque couche
c        (en entree : la valeur au debut du pas de temps)
c cd : cdrag
c      (en entree : la valeur au debut du pas de temps)
c q2 : $q^2$ au bas de chaque couche
c      (en entree : la valeur au debut du pas de temps)
c      (en sortie : la valeur a la fin du pas de temps)
c long : longueur de melange au bas de chaque couche
c        (en sortie : la valeur a la fin du pas de temps)
c km : diffusivite turbulent de quantite de mouvement (au bas de chaque
c      couche)
c      (en sortie : la valeur a la fin du pas de temps)
c kn : diffusivite turbulent des scalaires (au bas de chaque couche)
c      (en sortie : la valeur a la fin du pas de temps)
c
c.....................................................................
```

3 New radiation scheme design

3.1 Introduction

The representation of radiative transfers in Mars atmosphere require a modeling of CO2 gas and airborn dust optical properties. GCM simulations require that these properties are accurately represented at low computational expenses. CO2 gas infrared emission and absorption properties are well known and accurate parametrisation schemes are available for the complex line spectrum of the $15\mu m$ band (Hourdin, 1992). Such parametrisations insure that GCM simulations are realistic for clear conditions were CO2 effects are widely dominant. Parametrisation of dust radiative properties is however given less attention in the GCM literature.

The object of the present text is to describe the parametrisation schemes used in LMD and AOPP GCMs for representation of absorption, emission and scattering properties of airborn dust. This includes discussions of solar and infrared spectral data, spectral discretisations and numerical integration procedures.

3.2 Dust absorption and scattering at solar wavelengths

3.2.1 Spectral data

Measurements of the sky brightness above Viking Lander 1 and 2 have been used to infer the dust single scattering properties ω_0 and g at visible wavelength. The dataset, originally analyzed by Pollack et al. (1979), has been recently and more accurately reanalyzed by Pollack et al. (1995). Ockert-Bell et al. (1994, 1996) have extended the Pollack et al. (1995) data over the solar wavelengths using the composite spectra of the Martian soil from Mustard and Bell (1994). This dataset has been successfully validated by simulating the reflectance observed with the Viking IRTM solar channel during the dust storms. Thus, we have chosen to use these optical constants in the GCM. Fig. 1 show the dust scattering parameters deduced from this study. They are characterized by an abrupt change of the single scattering albedo ω and the asymmetry parameter g around 0.5 μm, near the peak of the incident solar flux.

3.2.2 Numerical integration

The numerical scheme used for integration of the radiative transfer equation (including scattering) at solar wavelengths is that of Fouquart and Bonel (1980). The questions that arise for use of the spectral data described in the previous paragraph are : i) the choice of a wide band spectral discretisation ; ii) the computation of average optical properties for each spectral band. Ockert-Bell et al. (1994) have shown that, because of the change near 0.5 μm, multispectral calculations were essential to obtain accurate results. Since detailed multispectral calculations would be too expensive in a GCM, we use two broad bands : [0.1 μm - 0.5 μm] and [0.5 μm - 5 μm]. The computation of average optical properties is performed according to the following ponderation laws :

$$\overline{Q}_{ext} = \frac{\int_{\lambda_1}^{\lambda_2} S_\lambda Q_{ext,\lambda} d\lambda}{\int_{\lambda_1}^{\lambda_2} S_\lambda d\lambda} \tag{25}$$

$$\overline{\omega} = \frac{\int_{\lambda_1}^{\lambda_2} S_\lambda Q_{ext,\lambda} \omega_\lambda d\lambda}{\int_{\lambda_1}^{\lambda_2} S_\lambda Q_{ext,\lambda} d\lambda} \tag{26}$$

and

$$\overline{Q}_{ext} = \frac{\int_{\lambda_1}^{\lambda_2} S_\lambda Q_{ext,\lambda} \omega_\lambda g_\lambda d\lambda}{\int_{\lambda_1}^{\lambda_2} S_\lambda Q_{ext,\lambda} \omega_\lambda d\lambda} \tag{27}$$

where Q_{ext} is the extinction parameter, S is the solar radiance and λ_1 and λ_1 are the wavelength boundaries of the considered spectral band.

3.3 Dust absorption and scattering at infrared wavelengths

3.3.1 Spectral data

Several models of dust radiative properties at thermal wavelengths have been proposed in the literature (Toon et al., 1977, Clancy et al., 1995). However, most of them were designed to study the size or the composition of the dust particles rather than their impact on the radiative budget: the basic approach has been to assume that the optical indices were described by known Earth mineral or soil type. For instance, the long-standing Toon et al. (1977) model of Mars atmospheric dust is based on the use of the optical properties of a clay mineral sample called montmorillonite 219b. Unfortunately, none of these models can accurately reproduce the

observation (e.g. the IRIS spectra obtained during the 1971 dust storm), especially around 20 μm where the blackbody emission is close to its maximum at Martian temperatures.

Therefore, we have decided to design a "synthetic" dust model, without concern for the actual dust composition. Because the size distribution and the composition suggested by Toon et al. was able to match the observed 9-μm absorption band, we have chosen to base the new model on their model below 15 μm, and to improve it at wavelengths above 15 μm. The optical constant of Toon et al. montmorillonite 219b are shown in Fig. 2. The corresponding scattering parameters, deduced from the Mie theory using a modified-gamma size distribution with a cross-section weighted mean radius r_{eff}=2.7 μm and variance ν_{eff}=0.4 μm, are presented in Fig. 3. The montmorillonite 219b is characterized by two absorption bands at 19 and 21 μm. Such bands are not apparent in the IRIS spectra of Mars atmospheric dust. In fact, unlike the Si-O stretching fundamental band near 9-10 μm which appears in most silicates, these bands are not universal. In particular, measurements by Roush et al. (1991) have shown that some minerals thought to be close to the Martian minerals (palagonite, saponite) do not exhibit such bands. However, most of these minerals, including montmorillonite, are characterized by a real index of refraction near 2.2 beyond 30 μm.

Based on these considerations, we have tried to reproduce the IRIS observations by removing the montmorillonite bands near 20 μm, and by keeping the real index constant at 2.2 above 17 μm. In fact, very good results can be obtained with an imaginary index set constant (0.5) over the same spectral region. This very simple synthetic dust model and the corresponding scattering properties are shown along with the Toon et al. data in Fig. 2 and Fig. 3.

The scaling of dust opacity in the infrared compared to the visible is also a key parameter in the model since it controls the local radiative balance of the atmosphere. Martin (1986) compared his IRTM 9 μm opacity determinations over the two Viking Landers sites with the lander solar extinction observations (Colburn et al., 1989). He determined a $\frac{\tau_{0.67\mu m}}{\tau_{9\mu m}}$ ratio of 2.5. This value is supported by separate analyses of the IRTM emission-phase-function visible and 9-μm sequences (Clancy et al., 1995).

The ability of this new model to reproduce the observations is shown in Fig. 4. Four IRIS spectra, typical of dusty conditions, are compared with numerical simulation results based on the original Toon et al. montmorillonite 219b and our new synthetic model. The numerical scheme used for this comparison is the numerical scheme implemented in the GCM (see next paragraph) ; the only difference is that it is used here with a fine spectral discretisation whereas a wide band discretisation is used for GCM simulations. The conclusions of this comparison are : i) the new data set improves greatly the fit with observations ; ii) the numerical scheme represents accurately dust emission, absorption and scattering phenomena.

3.3.2 Numerical integration

Two distinct numerical schemes are used for integration of the radiative transfer equation at infrared wavelengths. The CO2 15 μm band, that extends from 11.6 μm to 20.0 μm, is treated with the numerical scheme of Hourdin (1992) : this scheme requires the knowledge of average spectral properties of dust that are computed from the spectral data proposed in the preceding paragraph :

$$\overline{Q}_{ext} = \frac{\int_{\lambda_1}^{\lambda_2} B_\lambda Q_{ext,\lambda} d\lambda}{\int_{\lambda_1}^{\lambda_2} B_\lambda d\lambda} \tag{28}$$

$$\overline{\omega} = \frac{\int_{\lambda_1}^{\lambda_2} B_\lambda Q_{ext,\lambda} \omega_\lambda d\lambda}{\int_{\lambda_1}^{\lambda_2} B_\lambda Q_{ext,\lambda} d\lambda} \tag{29}$$

and

$$\overline{Q}_{abs} = (1 - \overline{\omega})\overline{Q}_{ext} \tag{30}$$

where B is the blackbody intensity at 215K, λ_1 and λ_2 are the limit wavelengths of the CO2 15 μm band and Q_{abs} is single absorption extinction parameter.

Outside the CO2 15 μm band, it is assumed that airborn dust is the only optical participant. The radiative transfer equation is solved in a way that accurately represents scattering of infrared light by dust particles. This scheme is described in Toon et al. (1989) . The infrared spectrum (outside the CO2 15 μm band) is dicretised in two wide bands : one band for the 9 μm band that extends from 5 μm to the lower limit of the CO2 band ; one band for the rest of the infrared spectrum (from the upper limit of the CO2 band to 200 μm). For each band, the average values of the extinction parameter and single scattering albedo are computed with Eq. 28 and Eq. 29. The average asymmetry factor is computed as

$$\overline{g} = \frac{\int_{\lambda_1}^{\lambda_2} B_\lambda Q_{ext,\lambda} \omega_\lambda g_\lambda d\lambda}{\int_{\lambda_1}^{\lambda_2} B_\lambda Q_{ext,\lambda} \omega_\lambda d\lambda} \tag{31}$$

It was checked that this discretisation in two wide bands introduces less than 10% error compared to a more sophisticated narrow band computation.

3.4 Computational aspects

The major change in terms of computational aspects is the addition of the routine flusv.f that computes infrared radiative transfers including scattering effects. flusv.f is called by radite.f :

```
      SUBROUTINE flusv(ngrid,nsf,n,omega,g,tau,emis,bh,bsol,fah,fdh)
      IMPLICIT NONE
c.....................................................................
c
c  calcul des flux ascendant et descendant aux interfaces entre n couches
c  * dans l'infrarouge
c  * B est une fonction lineaire de $\tau$ a l'interieur de chaque couche
c  * le B du sol peut etre different de celui qui correspond au profil
c    de la n-ieme couche
c  * l'hypothese est une hypothese a deux flux isotropes sur chaque
c    hemisphere ("hemispheric constant") + "source function technique"
c    (voir Toon et al. 1988)
c  * le flux descendant en haut de l'atmosphere est nul
c  * les couches sont numerotees du haut de l'atmosphere vers le sol
c
c  in :   * ngrid      ---> dimension de vectorisation
c         * nsf        ---> nsf=0 ==> "hemispheric constant"
c                           nsf>0 ==> "hemispheric constant" + "source function"
c         * n          ---> nombre de couches
c         * omega(i)   ---> single scattering albedo pour la i-eme couche
c         * g(i)       ---> asymmetry parameter pour la i-eme couche
c         * tau(i)     ---> epaisseur optique de la i-eme couche
c         * emis       ---> emissivite du sol
```

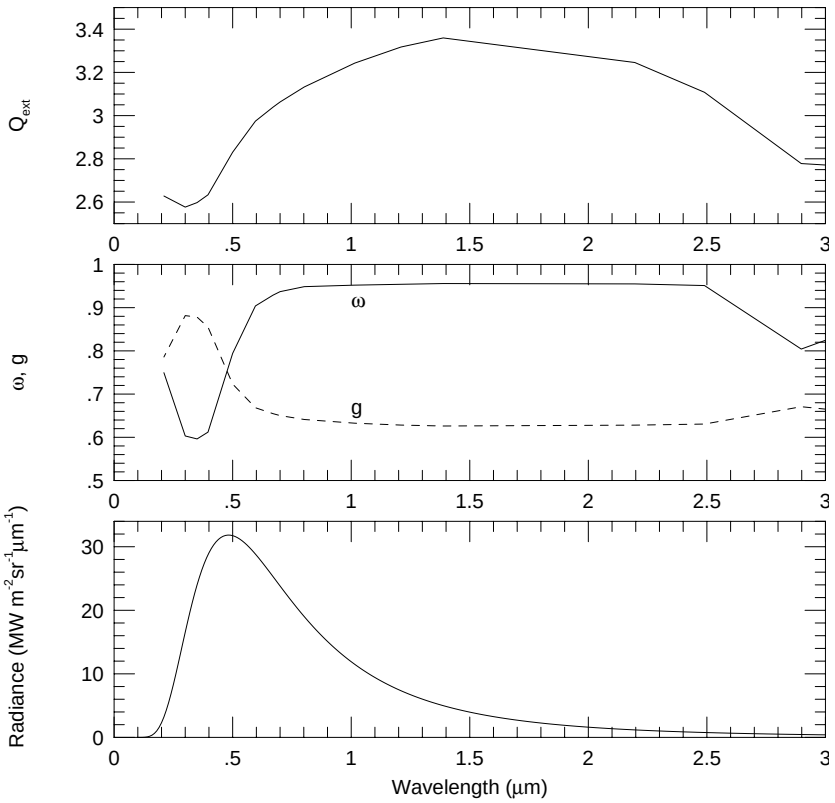

Figure 1: Martian dust single scattering properties at solar wavelength used to compute the wavelength integrated parameters in the GCM (from Ockert-Bell et al. ,1996). Q_{ext} is the extinction parameter, ω the single scattering albedo and g the asymmetry parameter. Also shown is the radiance of a blackbody at 6000 K, illustrating the incident solar radiation at the top of the atmosphere.

```
c          * bh(i)      ---> luminance du corps noir en haut de la i-eme
c                           couche, bh(n+1) pour la valeur au sol qui
c                           correspond au profil de la n-ieme couche
c          * bsol       ---> luminance du corps noir au sol
c
c  out :  * fah(i)      ---> flux ascendant en haut de la i-eme couche,
c                           fah(n+1) pour le sol
c          * fdh(i)     ---> flux descendant en haut de la i-eme couche,
c                           fdh(n+1) pour le sol
c
c.....................................................................
```

4 Representation of Sub-Grid Scale Orography

4.1 Introduction

The orography used in the GCM is smoothed to the horizontal resolution of the model i.e. variations of orography below the grid scale are effectively ignored. These sub-grid scale variations can, however, have a significant impact on the circulation of

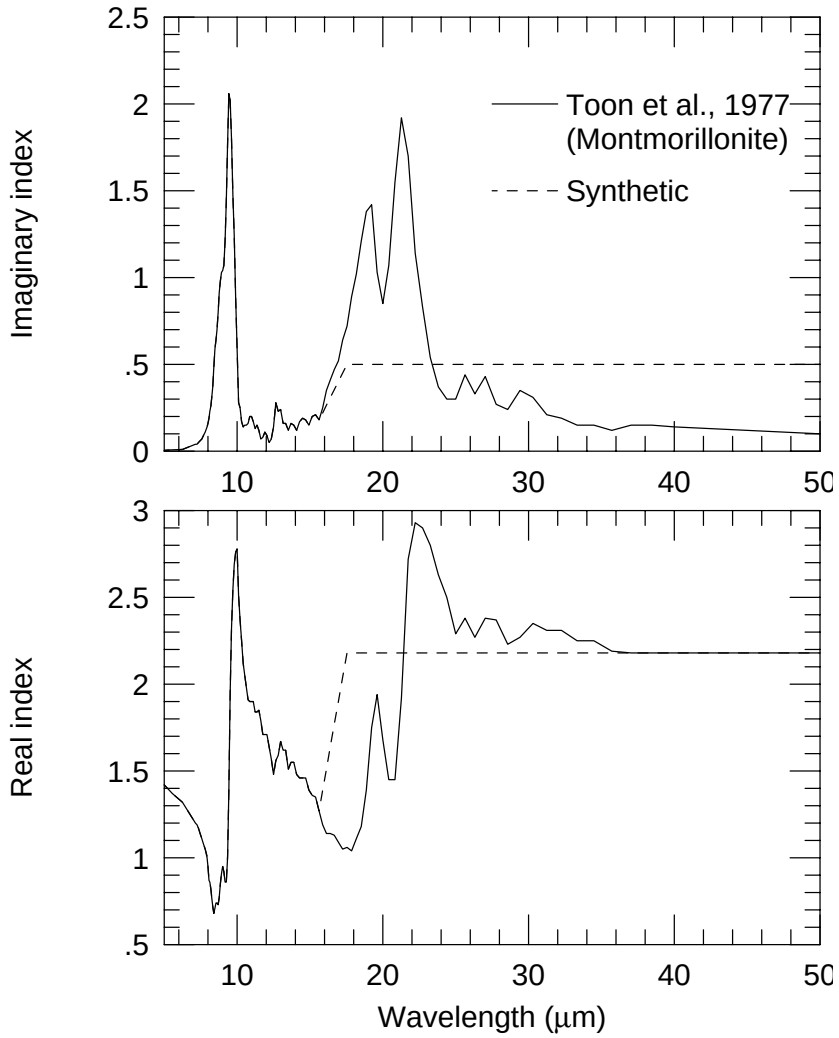

Figure 2: Optical constant of our "synthetic" model compared to the Toon et al. (1977) montmorillonite 219b.

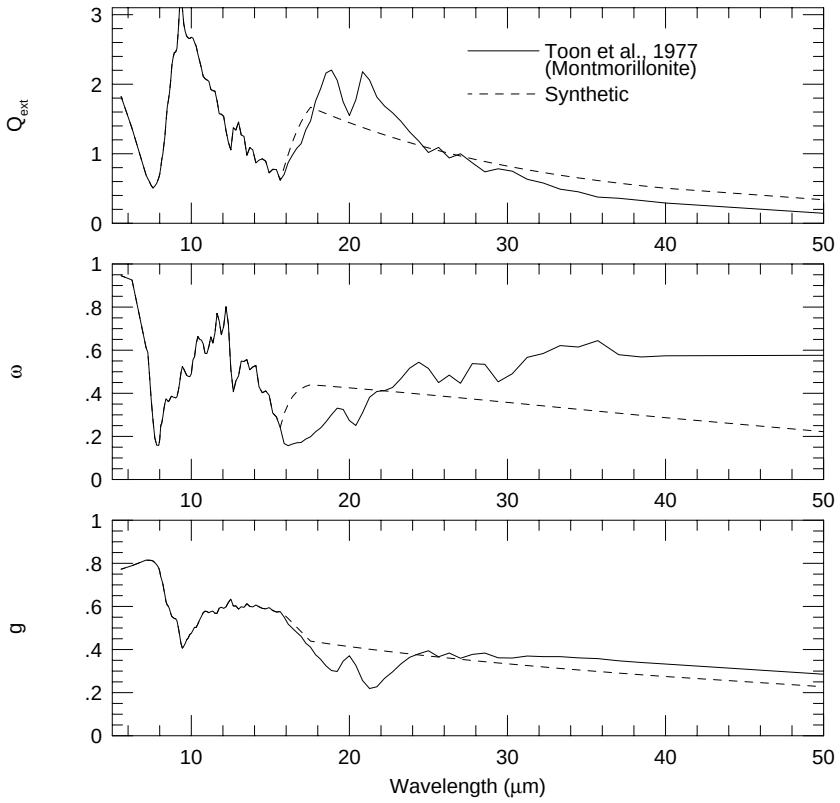

Figure 3: Martian dust single scattering properties at thermal wavelength of our synthetic model compared to the Toon et al. (1977) model. Both use a modified-gamma size distribution with r_{eff}=2.7 μm and ν_{eff}=0.4 μm. Q_{ext} is the extinction parameter, ω the single scattering albedo and g the asymmetry parameter. The synthetic parameters are used to compute the wavelength integrated parameters in the GCM.

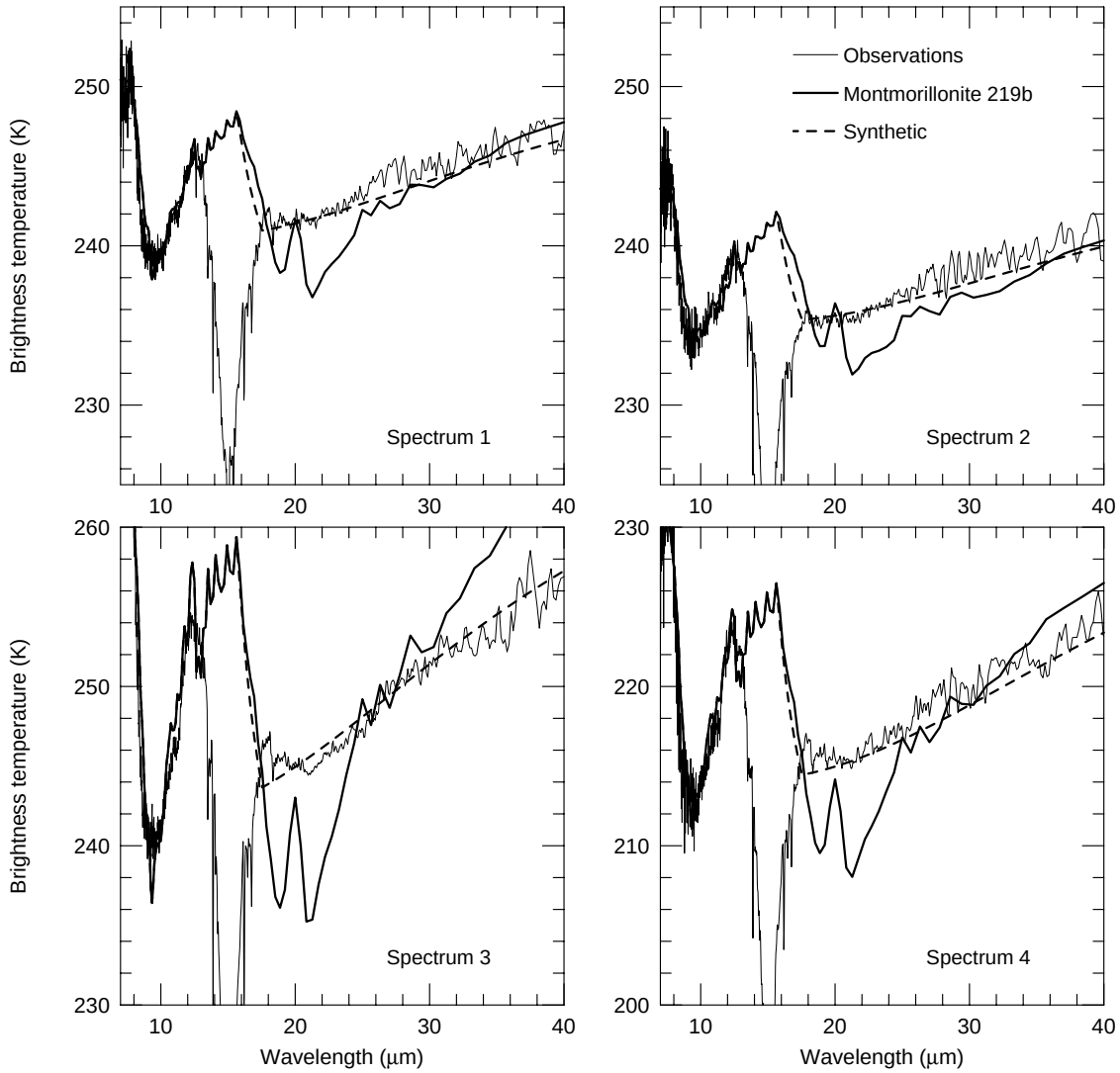

Figure 4: Model brightness temperature spectra computed with the Toon et al. (1977) model and our new synthetic model are compared to four Mariner 9 spectra obtained during the 1971 dust storms. These IRIS spectra had been selected by Clancy et al. (1995) because they are representative of the dust signatures observed then. The radiative transfer model used for the simulation is similar to the dust model now used in the GCM (although much more spectral bands are used). Temperatures profiles were estimated for each IRIS spectra by inversing the CO_2 15-μm band with the narrow-band model developed by Hourdin(1992).

the atmosphere, so their effect must be parametrised in some way. More specifically the sub-grid scale mountains can influence the model scale flow in two ways, (a) by producing a form drag on the flow at low levels, and (b) by exciting internal gravity waves which can propagate in the vertical, break, and decelerate the flow far away from the mountains themselves. We have chosen to parametrise these two effects using, for (a), the low level drag scheme of **?** and for (b) the gravity wave drag scheme of Miller et al. (1989) and Baines and Palmer (1990) which was developed from the Palmer et al. (1986) scheme. Both these schemes are state of the art and are in current operational use at the European Centre for Medium Range Weather Forecasting.

4.2 Low Level Drag Parametrisation

A complete account of the low level drag parametrisation scheme, together with its validation against observations and an account of its performance in the ECMWF forecast model, can be found in **?**. The details of the scheme are reproduced here for completeness.

We define the non-dimensional height of a single mountain, H_N, as

$$H_N \;=\; \frac{NH}{|U|} \tag{32}$$

where H is the maximum height of the mountain, U is the speed of the wind incident on the mountain and N is the Brunt-Viäsälä frequency.

At small H_N all the air flows over the mountain and gravity waves are generated (see section 4.3). There is no low level flow drag in this case. At large H_N part of the low level air flow goes around the mountain producing a drag on the low level flow. Figure 5 shows a schematic of the flow at large H_N.

The drag, D, on the low level flow can be written as

$$D(z) \;=\; -\,\rho\, C_d\, l(z)\, \frac{u|u|}{2} \tag{33}$$

where ρ is the density, $l(z)$ is a length scale based on the horizontal scale of the intersection of the mountain with the incident flow, and C_d is a drag coefficient of order unity. For an elliptical mountain, i.e.

$$h \;=\; \frac{h}{1+\dfrac{x^2}{a^2}+\dfrac{y^2}{b^2}} \;:\; b>a \tag{34}$$

then

$$l(z) \;=\; 2b\sqrt{\frac{Z_b - z}{z}} \tag{35}$$

where Z_b is the upstream elevation of the lowest isentrope that goes over the mountain (see fig. 5). Z_b can be written as

$$Z_b \;=\; H\frac{(H_N - H_{NC})}{H_N} \tag{36}$$

where H_{NC} is a critical non-dimensional mountain height of order unity.

In a GCM grid box there is often more than one mountain and we must take account of this. At a given altitude, z, the intersection between the mountains and the model layer approximates to an ellipsoid of eccentricity

$$(a', b') \;=\; (a, b)\sqrt{\frac{Z_b - z}{z+\mu}} \tag{37}$$

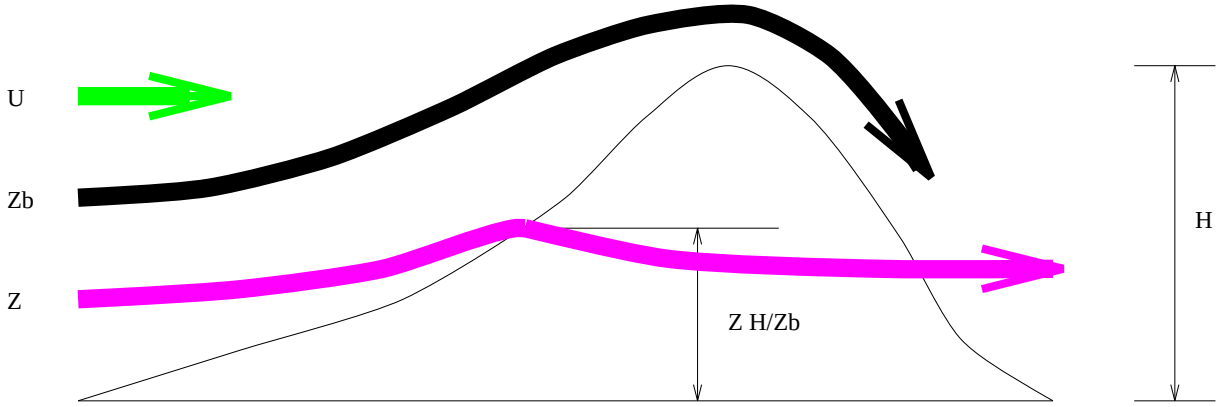

Figure 5: Schematic representation of the low level flow behaviour in sub-grid scale orographic drag parametrisation scheme.

where μ is the standard deviation of the sub-grid scale orography (see section 4.4 and fig. 7). Then $l(z)$ can be written approximately as

$$l(z) \;=\; 2\max(b\cos\psi, a\sin\psi)\sqrt{\frac{Z_b - z}{z+\mu}} \tag{38}$$

where ψ is the angle between the incident flow and the normal ridge direction θ (see section 4.4 and fig. 9). We note that if L is the width of the grid box, then for $\psi = 0$ there are $L/2a$ ridges in the box and for $\psi = \pi/2$ there are $L/2b$ ridges in the box. Hence

$$l(z) \;=\; \frac{L^2}{2}\sqrt{\frac{Z_b - z}{z+\mu}}\max\left(\frac{\cos\psi}{a}, \frac{\sin\psi}{b}\right). \tag{39}$$

If σ is the anisotropy of the orography and γ is the slope (see section 4.4 and figs. 10 and 8) we note that $a \approx \mu/\sigma$ and $a/b \approx \gamma$ hence the model low level drag is

$$D(z) \;=\; -C_d\max(2 - \frac{1}{r}, 0)\rho\frac{\sigma}{2\mu}\sqrt{\frac{Z_b - z}{z+\mu}}\max\left(\frac{\cos\psi}{a}, \frac{\sin\psi}{b}\right)\frac{U|U|}{2} \tag{40}$$

where

$$r \;=\; \frac{\cos^2\psi + \gamma\sin^2\psi}{\gamma\cos^2\psi + \sin^2\psi} \tag{41}$$

For convenience, and for consistency with the gravity wave drag scheme (section 4.3) we substitute the function $B\cos^2\psi + C\sin^2\psi$, ($B$ and C are defined in section 4.3) for the expression $\max\left(\frac{\cos\psi}{a}, \frac{\sin\psi}{b}\right)$. In the GCM the term $D(z)$ is evaluated quasi-implicitly in ensure numerical stability.

The tunable parameters in the scheme are the critical non-dimensional mountain height, H_{NC}, and the drag coefficient, C_d.

4.3 Gravity Wave Drag

Full details of the scheme are given in **?**, Miller et al. (1989), Baines and Palmer (1990) and Palmer et al. (1986) but the essentials are reproduced here for completeness. It is common in parametrising gravity wave drag to assume a single gravity wave, with some characteristic wavelength, that propagates from the surface of the model only in the vertical plane. Schemes that represent ensembles of gravity wave

schemes are computationally very expensive and, as yet, little tested in terrestrial climate models.

The vector surface stress induced by a single gravity wave generated by a single elliptical mountain, of the form given by equation (34), can be written as (Phillips, 1984)

$$\tau \;=\; \rho\, U\, N\, H^2\, b\, G\, (B\cos^2\psi + C\sin^2\psi, (B-C)\sin\psi\cos\psi) \tag{42}$$

where $B = 1 - 0.18\gamma - 0.04\gamma^2$, $C = 0.48\gamma + 0.3\gamma^2$, G is a constant of order unity and all the other symbols are as defined in section 4.2. Summing over all mountains in the grid box the model gravity wave stress becomes

$$\tau \;=\; \rho\, U\, N\, \mu\, \sigma\, G\, (B\cos^2\psi + C\sin^2\psi, (B-C)\sin\psi\cos\psi). \tag{43}$$

We now consider what happens when the gravity wave propagates vertically. We assume that the stress at any level is parallel to the surface stress and can be written

$$\tau \;=\; |\tau| \;=\; \kappa\, \rho\, U\, N\, \delta h^2 \tag{44}$$

where $\kappa \;=\; \mu\sigma G|(B\cos^2\psi + C\sin^2\psi, (B-C)\sin\psi\cos\psi)|$ and δh can be thought of as the vertical isentropic displacement induced by the propagating gravity wave. We then judge the effect of the wave on the mean flow by calculating the minimum Richardson number attainable i.e. the Richardson number that is 'felt by the gravity wave'.

$$Ri_{min} \;=\; Ri \frac{1 - \dfrac{N\,\delta h}{U}}{\left(1 + Ri^{1/2}\,\dfrac{N\,\delta h}{U}\right)^2}. \tag{45}$$

Following Lindzen (1981) the saturation hypothesis is employed. When Ri_{min} is greater than some critical value, Ri_c, the stress remains constant with height, the gravity wave continues to propagate vertically and Ri_{min} is evaluated at the next model level. This is repeated until Ri_{min} drops below the critical value, Ri_c, and the wave is deemed to have broken. Then a new value for the isentropic displacement, δh, and hence a new value for the stress, is calculated in order to keep $Ri_{min} \;=\; Ri_c$. The whole process is repeated until the top of the model is reached and the stress is assumed to be zero i.e. the waves are assumed to be dissipated somewhere in the atmosphere. The tendencies are calculated from the vertical derivative of the stress profile. A schematic diagram of the gravity wave drag algorithm is shown in fig. 6.

The scheme represents stationary wave critical level absorption, as when the component of the wind in the direction of the surface stress approaches zero the Richardson number becomes very large causing the wave amplitude to become very small. The wave is thus absorbed at the critical level and the stress set to zero above the critical line.

The tunable parameters for the scheme are G, which multiplies the expression for the gravity wave surface stress, and Ri_c, the critical Richardson number.

.

4.4 Sub-grid Scale Orographic Parameters

As has already been indicated (sections 4.2 and 4.3), the sub-grid scale orography is specified by 4 parameters; the standard deviation within the grid box, μ, the anisotropy, γ, the angle of the principal axes of the orography, θ, and the slope parameter, σ (**?**Baines and Palmer, 1990). They are defined as follows. Let $h(x, y)$ be the orography within the grid box defined at N points and $\bar{h}$ be the mean orography, then

$$\mu \;=\; \frac{\sqrt{\sum (h - \bar{h})^2}}{N} \tag{46}$$

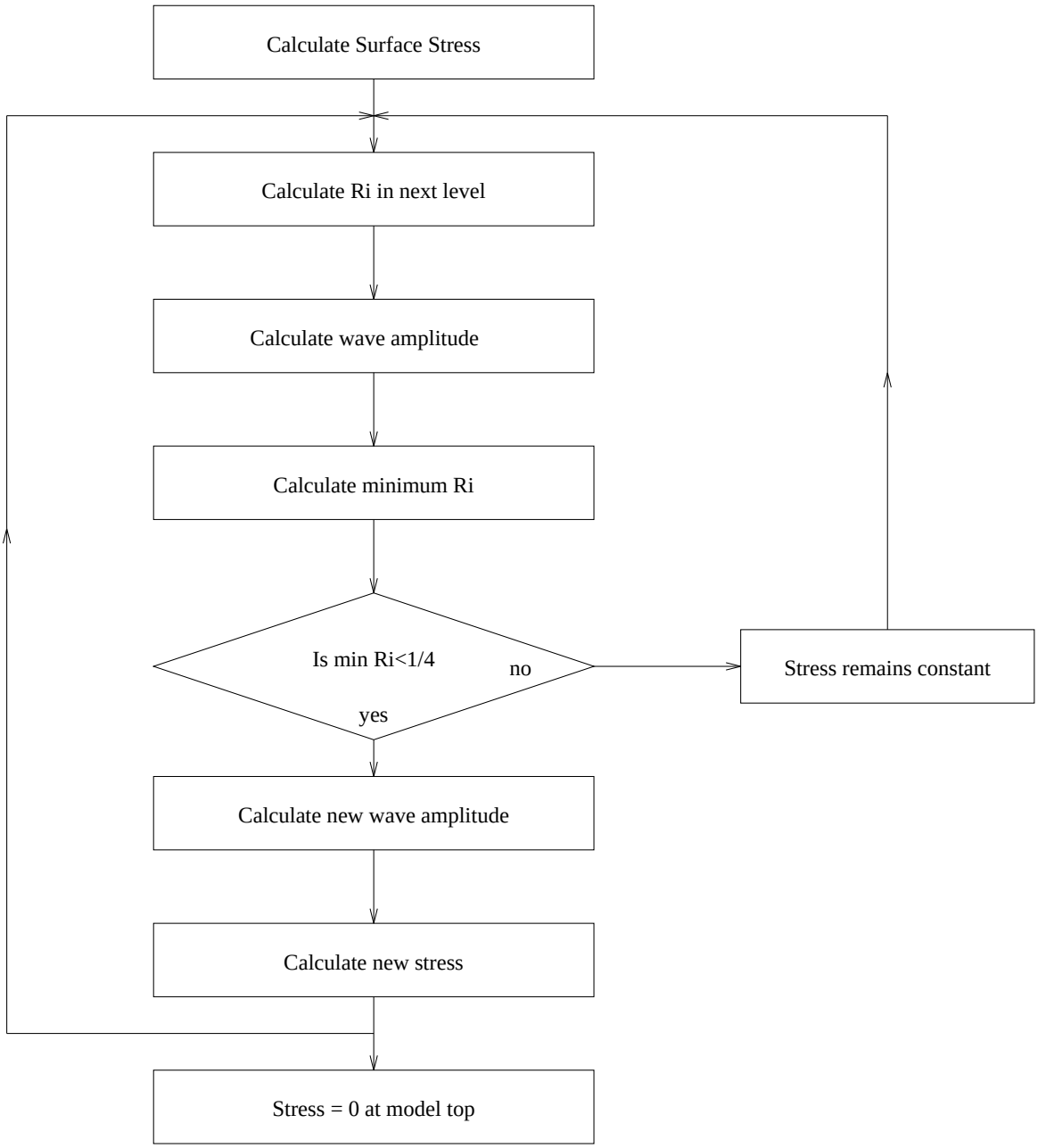

Figure 6: A schematic diagram of the gravity wave drag algorithm.

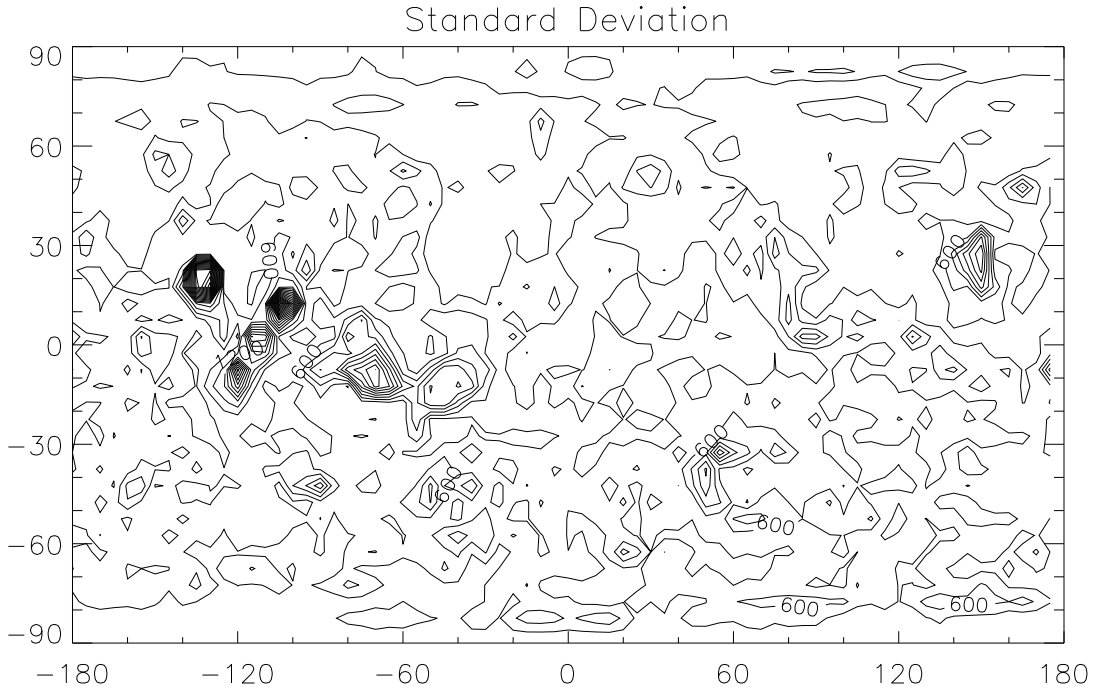

Figure 7: The sub-grid scale orographic standard deviation, μ. The contour interval is $300m$.

$$\theta = \frac{1}{2}\arctan\left(\frac{L}{M}\right) \tag{47}$$

where

$$M = \overline{\frac{\partial h}{\partial x}\frac{\partial h}{\partial u}} \tag{48}$$

and

$$L = \frac{1}{2}\left(\left(\frac{\partial h}{\partial x}\right)^2 - \left(\frac{\partial h}{\partial y}\right)^2\right). \tag{49}$$

The anisotropy is

$$\gamma = \sqrt{\left(\frac{\partial h}{\partial y'}\right)^2 \Big/ \left(\frac{\partial h}{\partial x'}\right)^2} \tag{50}$$

where

$$x' = x\cos\theta + y\sin\theta \tag{51}$$

and

$$y' = y\cos\theta - x\sin\theta, \tag{52}$$

and the slope parameter, σ, is defined by

$$\sigma^2 = \overline{\left(\frac{\partial h}{\partial x'}\right)^2} \tag{53}$$

These parameters have been calculated from the Mars Digital Topographic Map (Wu, 1981, DTM,) at $1^\circ \times 1^\circ$ degrees resolution and are shown in figures 7-10.

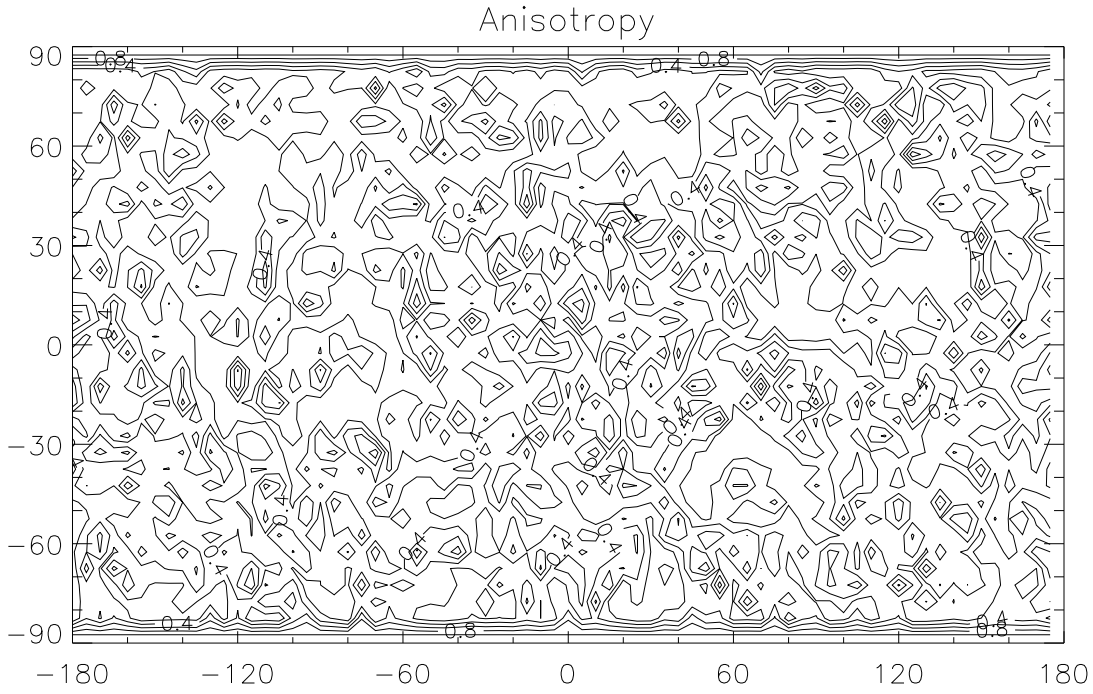

Figure 8: The sub-grid scale orographic anisotropy parameter, γ. The contour interval is 0.2.

4.5 Computational Aspects

The sub-grid scale orographic parametrisation subroutines are as follows

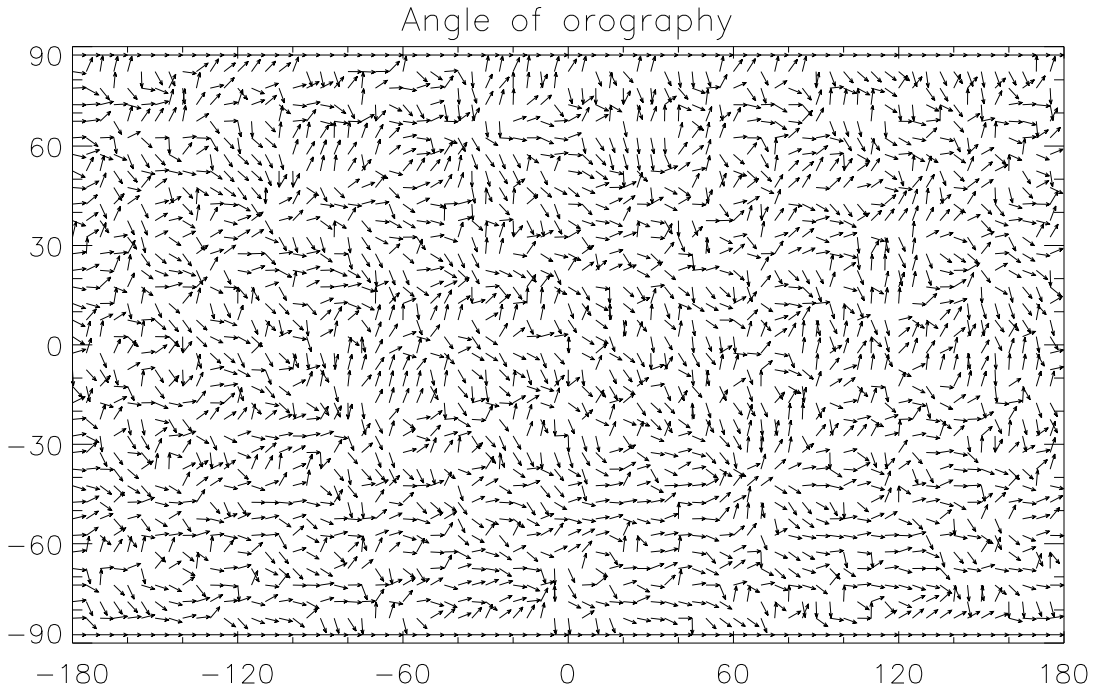

Figure 9: The angle of the principal axes of the sub-grid scale orography, θ, indicated by vectors.

Model file	Type	Description
`sugwd.f`	Subroutine	Sets various parameters for use in the scheme including the 4 legitimately tunable parameters shown in the table below.
`grid_noro.f`	Subroutine	Computes the sub-grid scale orographic parameters, μ, θ, γ and σ. See section 4.4 for their definitions.
`drag_noro.f`	Subroutine	Interface for the scheme. Zeros tendencies, computes geopotential height and updates the tendencies after the scheme has been called.
`orodrag.f`	Subroutine	Called from `drag_noro.f`. Main routine for the scheme. Computes the stress profile due to the gravity wave and due to the low level flow drag. Computes the tendencies as a vertical derivative of the stress profile.
`orosetup.f`	Subroutine	Called from `orodrag.f`. Computes basic state variables for the gravity wave drag component of the scheme.
`gwstress.f`	Subroutine	Called from `orodrag.f`. Computes surface stress due to the gravity wave.
`gwprofil.f`	Subroutine	Called from `orodrag.f`. Computes stress profile due to propagating gravity wave.
`yoegwd.h`	Common block	Stores various parameters for the scheme.
`surfdat.h`	Common block	Stores the sub-grid scale orographic parameters computed in `grid_noro.f`.

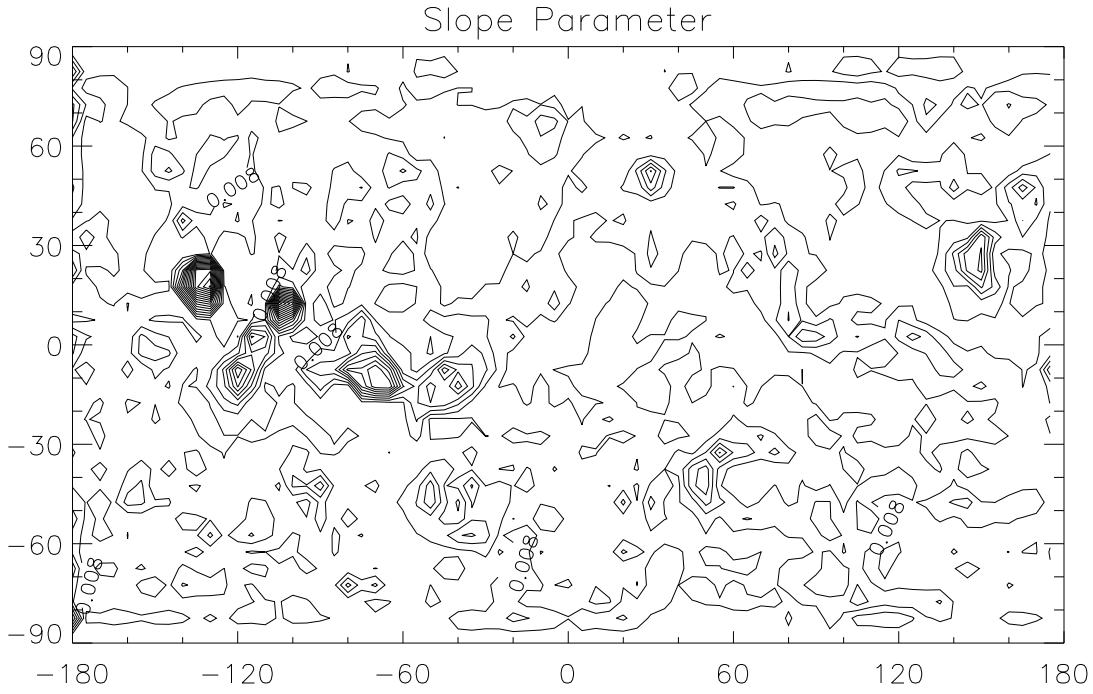

Figure 10: The sub-grid scale orographic slope parameter, σ. The contour interval is 0.004.

Main Subroutine Heads

```
SUBROUTINE drag_noro (nlon,nlev,dtime,pplay,pplev,
e pvar, psig, pgam, pthe,
e kgwd,kgwdim,kdx,ktest,
e t, u, v,
s pulow, pvlow, pustr, pvstr,
s d_t, d_u, d_v)
C**** *DRAG_NORO* INTERFACE FOR SUB-GRID SCALE OROGRAPHIC SCHEME
C
C PURPOSE.
C --------
C ZEROS TENDENCIES, COMPUTES GEOPOTENTIAL HEIGHT AND UPDATES THE
C TENDENCIES AFTER THE SCHEME HAS BEEN CALLED.
C
C EXPLICIT ARGUMENTS :
C --------------------
C
C INPUT :
C
C NLON : NUMBER OF HORIZONTAL GRID POINTS
C NLEV : NUMBER OF LEVELS
C DTIME : LENGTH OF TIME STEP
C PPLAY(NLON,NLEV+1) :  PRESSURE AT MIDDLE LEVELS
C PPLEV(NLON,NLEV) : PRESSURE ON MODEL LEVELS
C PVAR(NLON) : SUB-GRID SCALE STANDARD DEVIATION
```

```
C PSIG(NLON) : SUB-GRID SCALE SLOPE
C PGAM(NLON) : SUB-GRID SCALE ANISOTROPY
C PTHE(NLON) : SUB-GRID SCALE PRINCIPAL AXES ANGLE
C KGWD : NUMBER OF POINTS AT WHICH THE SCHEME IS CALLED
C KGWDIM : NUMBER OF POINTS AT WHICH THE SCHEME IS CALLED
C KDX(NLON) : POINTS AT WHICH TO CALL THE SCHEME
C KTEST(NLON) : MAP OF CALLING POINTS
C T(NLON,NLEV) : TEMPERATURE
C U(NLON,NLEV) : ZONAL WIND
C V(NLON,NLEV) : MERIDIONAL WIND
C
C OUTPUT :
C
C PULOW(NLON) : LOW LEVEL ZONAL WIND
C PVLOW(NLON) : LOW LEVEL MERIDIONAL WIND
C PUSTR(NLON) : LOW LEVEL ZONAL STRESS
C PVSTR(NLON) : LOW LEVEL MERIDIONAL STRESS
C D_T(NLON,NLEV) : TEMPERATURE TENDENCY
C D_U(NLON,NLEV) : ZONAL WIND TENDENCY
C D_V(NLON,NLEV) : MERIDIONAL WIND TENDENCY
C
C IMPLICIT ARGUMENTS :
C --------------------
C
C comcstfi.h
C dimphys.h
C

SUBROUTINE ORODRAG( NLON,NLEV
I , KGWD, KGWDIM, KDX, KTEST
R , PTSPHY
R , PAPHM1,PAPM1,PGEOM1,PTM1,PUM1
R , PVM1, PVAROR, PSIG, PGAMMA, PTHETA
C OUTPUTS
R , PULOW,PVLOW
R , PVOM,PVOL,PTE )
C
C
C**** *ORODRAG* - DOES THE GRAVITY WAVE PARAMETRIZATION.
C
C PURPOSE.
C --------
C
C THIS ROUTINE COMPUTES THE PHYSICAL TENDENCIES OF THE
C PROGNOSTIC VARIABLES U,V AND T DUE TO VERTICAL TRANSPORTS BY
C SUBGRIDSCALE OROGRAPHICALLY EXCITED GRAVITY WAVES
C
C EXPLICIT ARGUMENTS :
C --------------------
C
C INPUT :
C
C NLON : NUMBER OF HORIZONTAL GRID POINTS
C NLEV : NUMBER OF LEVELS
```

```
C KGWD : NUMBER OF POINTS AT WHICH THE SCHEME IS CALLED
C KGWDIM : NUMBER OF POINTS AT WHICH THE SCHEME IS CALLED
C KDX(NLON) : POINTS AT WHICH TO CALL THE SCHEME
C KTEST(NLON) : MAP OF CALLING POINTS
C PTSPHY : LENGTH OF TIME STEP
C PAPHM1(NLON,NLEV+1):  PRESSURE AT MIDDLE LEVELS
C PAPM1(NLON,NLEV) : PRESSURE ON MODEL LEVELS
C PGEOM1(NLON,NLEV) : GEOPOTENTIAL HIEGHT OF MODEL LEVELS
C PTM1(NLON,NLEV) : TEMPERATURE
C PUM1(NLON,NLEV) : ZONAL WIND
C PVM1(NLON,NLEV) : MERIDIONAL WIND
C PVAROR(NLON) : SUB-GRID SCALE STANDARD DEVIATION
C PSIG(NLON) : SUB-GRID SCALE SLOPE
C PGAMMA(NLON) : SUB-GRID SCALE ANISOTROPY
C PTHETA(NLON) : SUB-GRID SCALE PRINCIPAL AXES ANGLE
C
C OUTPUT :
C
C PULOW(NLON) : LOW LEVEL ZONAL WIND
C PVLOW(NLON) : LOW LEVEL MERIDIONAL WIND
C PVOM(NLON,NLEV) : ZONAL WIND TENDENCY
C PVOL(NLON,NLEV) : MERIDIONAL WIND TENDENCY
C PTE(NLON,NLEV) : TEMPERATURE TENDENCY
C
C IMPLICIT ARGUMENTS :
C --------------------
C
C comcstfi.h
C dimphys.h
C yoegwd.h
C
```

Default Parameter Settings

Variable name	Description	Default value
GKDRAG	Constant in gravity wave stress definition, G	0.1
GRCRIT	Critical Richardson number, Ri_c	0.25
GFRCRIT	Critical non-dimensional mountain height, H_{NC}	1.0
GKWAKE	Low level drag coefficient, C_d	1.0

5 CO_2 condensation-sublimation Scheme

5.1 introduction

The condensation and sublimation of the CO_2 atmosphere is locally controlled by relatively simple physical processes. When, on the ground or in the atmosphere, the local temperature fell below the condensation temperature, the CO_2 condense, releasing the latent heat required to keep the solid-gas interface at the condensation temperature. Conversely, when the CO_2 ice is heated, it partially sublimes to keep its temperature at the frost point temperature.

In the first version of the general circulation model, we had modeled these mechanisms rather straightforwardly. In particular, we had supposed that the CO_2 ice condensing up in the atmosphere was instantaneously precipitated onto the ground, without taking into account its altitude, its initial temperature and the

layers through which it was supposed to fall. This scheme gave rather good results [Hourdin et al., 1993, 1995] . However, we found that the impact of these simplifications was not negligible over the course of a Martian year. Within the context of the ESA contract, we have addressed this issue more carefully, paying especially attention to mass and energy balances.

5.2 Condensation in the atmosphere

Preliminary studies have shown that the formation of CO_2 ice particles in a CO_2 gas atmosphere was probably not limited by the cloud microphysical mechanisms which affect the formation of water clouds on Earth; e.g. supersaturation, nucleation, diffusion, etc... (Wood et al., 1995) . In fact, since no cloud microphysical model is yet available, we have made the following assumption : after condensing at a given level, the CO_2 ice instantaneously fell through the atmospheric layers located below, down to the ground.

In reality, the ice particles fell more slowly and may be horizontally advected by the wind. However, since the atmosphere keep condensing, and this preferentially on the CO_2 ice already formed, the particle size should readily increases. Because the sedimentation velocity is proportional to the square of the particles radius (Stockes'law), it is unlikely that the CO_2 ice may be transported over significant distances. Since the radiative properties of the clouds are taken into account elsewhere (see below), our assumption should not affect the condensation rate on the ground and in the atmosphere.

The CO_2 gas start condensing when the temperature T^* predicted by all the model parametrisations (condensation excepted) is below the condensation temperature Tc. The temperature T is then set to Tc. The corresponding energy deficit (in fact enthalpy deficit since the pressure forces are included) must be balanced by the CO_2 condensation. In the upper level of the model, the energy balance equation is :

$$c_p M_N (Tc_N - T^*_N) = L\delta m_N \tag{54}$$

With N the index of the upper layer, M_N the layer mass, c_p the specific heat at constant pressure (735.9 J kg^{-1} K^{-1} on Mars), L the CO_2 latent heat (5.9 10^5 J kg^{-1}), and δm_N the mass of ice that have condensed (>0 when condensing).

Below, the fact that the atmosphere might have condensed in the layers above must be taken into account. Considering that the layer l receives from the layer above $l+1$ the total amount of ice $\sum_{k=l+1}^{N} \delta m_k$, the energy balance equation for layer l can be written:

$$c_p M_l (Tc_l - T^*_l) = L\delta m_l + [g(z_{l+1} - z_l) + c_{ice}(Tc_{l+1} - Tc_l)] \sum_{k=l+1}^{N} \delta m_k \tag{55}$$

with z_l, Tc_l, T^*_l the altitude, the condensation temperature and the predicted temperature in the middle of layer l ; g the acceleration of gravity ; c_{ice} the specific heat of CO_2 ice (349+4.8T J kg^{-1} K^{-1}, with 73 K< T < 200 K, from Washburn [1948]).

The term $[g(z_{l+1} - z_l) \sum_{k=l+1}^{N} \delta m_k]$ corresponds to the potential energy released by the ice particles falling from layer l+1. The term $[c_{ice}(Tc_{l+1} - Tc_l) \sum_{k=l+1}^{N} \delta m_k]$, on the opposite, corresponds to the energy used to heat the masse $\sum_{k=l+1}^{N} \delta m_k$ from the temperature Tc_{l+1} to Tc_l. These two terms are not negligible: 1 kg of ice condensed at z = 10 km (about one atmospheric scale height) would release

$gz = 3.73\,10^4$ J and use $c_{ice}(Tc(z) - Tc(0)) \simeq -10^4$ J, respectively 6.3 and 1.7% of the latent heat initially released ($5.9\ 10^5$ J).

The amount of ice condensing in layer l during one timestep of the model will thus be :

$$\delta m_l = \frac{c_p M_l}{L}(Tc_l - T_l^*) - \frac{1}{L}[g(z_{l+1} - z_l) + c_{ice}(Tc_{l+1} - Tc_l)] \sum_{k=l+1}^{N} \delta m_k \qquad (56)$$

The ice condensed in the atmosphere can resublime during its descent if it encounters warmer layer. If the predicted temperature T_l is warmer than the condensation temperature Tc_l, equation 56 remains valid and the amount $\delta m_l < 0$ will be sublimed. However, if all the ice falling from the layers above sublimes in layer l (case when equation 56 predicts: $-\delta m_l > \sum_{k=l+1}^{N} \delta m_k$), we set $\delta m_l = -\sum_{k=l+1}^{N} \delta m_k$ and the layer temperature T_l is then given by:

$$T_l = T_l^* + \frac{1}{c_p M_l}[-L + g(z_{l+1} - z_l) + c_{ice}(Tc_{l+1} - Tc_l)] \sum_{k=l+1}^{N} \delta m_k \qquad (57)$$

5.3 Condensation and sublimation on the ground

The condensation on the ground is controlled by the same kind of equation than for the atmospheric condensation. The atmosphere just above the ground condenses to keep the surface temperature T_0 above the condensation temperature Tc_0. Conversely, the ice sublimes to keep $T_0 = Tc_0$ as long as solid CO_2 is present.

Equation 55 remains valid with $l = 0$ and replacing $c_p M_l$ by $c_s A$ with A the area of the grid point and c_s the surface heat capacity [1] (in J m^{-2} K^{-1}). The amount of ice condensed or sublimed on the ground δm_0 is therefore deduced from the temperature predicted before condensation T_0^* with :

$$\delta m_0 = \frac{c_s A}{L}(Tc_0 - T_0^*) - \frac{1}{L}[gz_1 + c_{ice}(Tc_1 - Tc_0)] \sum_{k=1}^{N} \delta m_k \qquad (58)$$

$\sum_{k=1}^{N} \delta m_k$ accounts for the amount of ice condensed in the atmosphere that reaches the ground. At every timestep, in the model, the mass $\sum_{k=0}^{N} \delta m_k$ is added to the amount of ice on the ground m_0. We set $T_0 = Tc_0$, unless the ground ice completely sublimes (case when equation 58 predict $-\delta m_0 > m_0 + \sum_{k=1}^{N} \delta m_k$). We then set $\delta m_0 = -m_0 - \sum_{k=1}^{N} \delta m_k$ and the surface temperature is expressed as:

$$T_0 = T_0^* - \frac{L}{C_s A} m_0 - \frac{1}{C_s A}[L - gz_1 - c_{ice}(Tc_1 - Tc_0)] \sum_{k=1}^{N} \delta m_k \qquad (59)$$

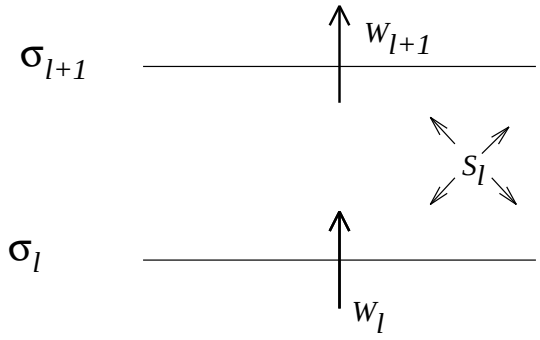

Figure 11: Masse balance in a layer l

5.4 Energy and mass balance in vertical coordinates σ=p/p_0

Le loss of atmospheric mass due to condensation (or conversely the gain due to sublimation) is taken into account by modifying the surface pressure at each timestep:

$$\delta p_0 = -\frac{g}{A}\sum_{k=0}^{N}\delta m_k \tag{60}$$

This ensures the conservation of the total mass of CO_2 (caps + atmosphere). However, in each layer, the mass transfer, the sources and the sinks created by the condensation-sublimation (and the corresponding heat and momentum transfers) requires a specific treatment. In particular, each layer is defined by its vertical coordinates $\sigma = p/p_0$. The changes in p_0 due to the CO_2 condensation-sublimation create an "artificial" movement of the σ levels in the atmosphere. This must be reflected in the temperatures and wind fields.

In a grid mesh of area A, the mass of a layer l delimited by the levels σ_l and σ_{l+1} (Fig. 11) is $M_l = \frac{A}{g}(\sigma_l - \sigma_{l+1})p_0$. The mass balance equation gives:

$$\frac{\partial M_l}{\partial t} = \frac{A}{g}(\sigma_l - \sigma_{l+1})\frac{\partial p_0}{\partial t} = W_l - W_{l+1} + S_l \tag{61}$$

where W_l is the mass flux (kg.s^{-1}) through the level σ_l (> 0 when up) and S_l the sources and sinks of CO_2 gas in the box l. S_l thus corresponds to the flux of condensed or sublimed CO_2. Because the sum of these fluxes creates the variations of the surface pressure p_0, we have :

$$\frac{\partial p_0}{\partial t} = \frac{g}{A}\sum_{k=0}^{N} S_k \tag{62}$$

In the model with timestep δt, we have by definition $S_l = -\delta m_l/\delta t$. A recursive formula can be deduced from equations 61 and 62 to compute the mass fluxes

[1]The surface heat capacity c_s has in fact a negligible impact on the amount of CO_2 ice condensed or sublimed δm_0. Indeed the surface temperature $T_0^*(t)$ predicted by all the model parametrisations (condensation excepted) is calculated from the previous timestep by:

$$T_0^*(t) = T_0(t-\delta t) + \frac{\sum F}{c_s A}\delta t$$

where $\sum F$ is the sum of the energy fluxes heating or cooling the ground. Thus, δm_0 does not generally depend upon c_s since, in equation 58, $\frac{c_s A}{L}(Tc_0 - T_0^*)$ is equal to $-\frac{\delta t}{L}\sum F$ when $T_0(t-\delta t) = Tc_0$.

between the layers due to the CO_2 condensation-sublimation:

$$W_{l+1} = W_l - \frac{\delta m_l}{\delta t} + (\sigma_l - \sigma_{l+1}) \sum_{k=0}^{N} \frac{\delta m_k}{\delta t} \tag{63}$$

with:

$$W_1 = -\frac{\delta m_0}{\delta t} \tag{64}$$

These mass fluxes are used to compute the exchange of heat and momentum between the layers. For c_pT (enthalpy), the advection equation can be written, (after elimination of c_p):

$$\frac{\partial M_l T_l}{\partial t} = W_l \overline{T_l} - W_{l+1} \overline{T_{l+1}} + S_l T c_l \tag{65}$$

$S_l T c_l$ corresponds to the enthalpy sources and sinks related to the mass of CO_2 gas sublimed or condensed. $\overline{T_l}$ is the mean temperature of the gas transported through the σ_l interface. Various operators have been suggested in the literature to calculate $\overline{T_l}$. Indeed, this process is similar to a classic transport process. In our case, we shall use a simple arithmetic average, $\overline{T_l} = (T_l + T_{l-1})/2$, with, on the ground, $\overline{T_1} = T_0$.

We also have, by definition:

$$\begin{aligned} \frac{\partial M_l T_l}{\partial t} &= M_l \frac{\partial T_l}{\partial t} + T_l \frac{\partial M_l}{\partial t} \\ &= \frac{A}{g}(\sigma_l - \sigma_{l+1}) p_0 \frac{\partial T_l}{\partial t} + T_l (W_l - W_{l+1} + S_l) \end{aligned} \tag{66}$$

From 65 et 66, the correction δT_l to be applied at every timestep in each layer after the CO_2 condensation sublimation is obtained:

$$\delta T_l = \frac{g}{A(\sigma_l - \sigma_{l+1}) p_0} [W_l \delta t (\overline{T_l} - T_l) - W_{l+1} \delta t (\overline{T_{l+1}} - T_l) + \delta m_l (T c_l - T_l)] \tag{67}$$

The first two terms, with W_l and W_{l+1}, corresponds to the re-arrangement of the températures over the entire column due to the pressure variations in σ coordinates. The last term $\delta m_l (T c_l - T_l)$ is usually equal to zero when the CO_2 condenses or partially sublimes since we then have $T c_l = T_l$. However, when the CO_2 totally sublimes (case of the equation 57), it becomes a cooling term accounting for the mixing of the newly sublimed mass $-\delta m_l$ with the rest of the layer at $T_l > T c_l$.

In the lower layer, equation 67 can be rewritten:

$$\delta T_1 = \frac{g}{A(1 - \sigma_2) p_0} [-\delta m_0 (T_0 - T_1) - W_2 \delta t (\overline{T_2} - T_1) + \delta m_1 (T c_1 - T_1)] \tag{68}$$

The term $\delta m_0 (T_0 - T_1)$ corresponds to the condensation-sublimation flux from the ground. This term can be considerable during the sublimation phase in spring and summer, when the temperature difference between the lower atmosphere and the ground reaches 50 K. The cooling of the first layer by the newly sublimed CO_2 is then comparable to a loss of energy $c_p(T_0 - T_1)/L \simeq 6\%$ of the latent heat initially required.

Similarly, the momentum distribution must be re-arranged, although condensation and sublimation cannot be considered as sinks or sources of momentum. For a wind component v, we shall simply write:

$$\delta v_l = \frac{g\delta t}{A(\sigma_l - \sigma_{l+1})p_0}[W_l(\overline{v_l} - v_l) - W_{l+1}(\overline{v_{l+1}} - v_l)] \quad (69)$$

with, on the ground, $\overline{v_1} = v_l$ si $\delta m_0 > 0$ and $\overline{v_1} = 0$ si $\delta m_0 < 0$ (the velocity of the CO_2 gas that has just sublimed is zero).

5.5 Computational aspect

The new CO_2 condensation-sublimation scheme subroutine `newcondens` is called by the main subroutine of the physical package `physiq`:

```
      SUBROUTINE newcondens(ngrid,nlayer,ptimestep,
     $                  pcapcal,pplay,pplev,ptsrf,pt,
     $                  pphi,pdt,pdtsrf,pu,pv,paerosol,
     $                  piceco2,psolaralb,pemisurf,
     $                  pdtc,pdtsrfc,pdpsrf,pdu,pdv,
     $                  pdaerosol)

       IMPLICIT NONE
c=======================================================================
c     Compute the  the CO2 condensation sublimation rate,
c     the impact of surface pressure changes in sigma coordinates
c
c     Call co2snow  (impact of the CO2 snow fall on the radiative budget)
c=======================================================================



c    input:
c   ------
c    ngrid                number of grid point in the horizontal physical grid
c    nlayer               number of layers
c    ptimestep            physical timestep (s)
c    pcapcal              surface heat capacity
c    pplay(ngrid,nlayer)  Pressure levels (mid layer)
c    pplev(ngrid,nlayer+1) Pressure levels (interface)
c    ptsrf(ngrid)         surface temperature
c    pt(ngrid,nlayer)     temperature (K)
c    pphi(ngrid,nlayer)   geopotentiel
c
c
c    pdt(ngrid,nlayer)  | time derivative before condensation
c    pdtsrf(ngrid)      | for pt and ptsrf
c    pu(ngrid,nlayer)     zonal wind
c    pv(ngrid,nlayer)     Merid wind
c    paerosol(ngrid,nlayer) Dust optical depth in each box
c
c   Input / output
c   --------------
c
c    piceco2(ngrid) :     Mass of CO2 on the ground (kg/m2)
c    psolaralb(ngrid,2) :  surface albedo
c    pemisurf(ngrid)    : surface emissivity
c
```

```
c   output:
c   -------
c
c    pdpsrf(ngrid)        |   Time derivative dur to the
c    pdtc(ngrid,nlayermx) |   condensation or sublimation)
c    pdtsrfc(ngrid)       |   for Ps,pt,ptsrf, pu,pv
c    pdu (ngrid,nlayer)   !
c    pdv (ngrid,nlayer)   |

c    pdaerosol            | not used in the ESA project

c=======================================================
c
c    Implicit argument
c    -----------------
c
#include "dimensions.h"
#include "dimphys.h"
#include "comcstfi.h"
#include "surfdat.h"
#include "comgeomfi.h"
#include "comvert.h"
```

6 The "CO_2 snow scheme: Modeling the impact of the CO_2 clouds and fresh snow on the radiative budget

6.1 Introduction: Clouds or snow?

The thermal Infrared instruments aboard Viking and Mariner 9 have shown that the CO_2 condensation rate was strongly reduced by some processes locally decreasing the infrared emission toward space (Forget et al., 1996). The location and brightness temperatures of these areas, also called "low emission zones", sometimes varied on time scales of days [*Kieffer et al.*, 1977]. Forget et al. (1995) used a combination of radiative transfer modeling and infrared data analysis to show that the low brightness temperatures were likely to be created by the radiative properties of CO_2 ice particle when these particles where formed up in the atmosphere rather than directly on the ground (Fig. 12). In that case, the infrared emission is decreased because the CO_2 snow grains can be efficient scatterers at infrared wavelengths, whether they are airborne (precipitating clouds) or on the ground (fresh snow).

The available observations do not permit to distinguish the impact of the clouds from the fresh snow effects. We do not know which process actually creates the low emission zones. Since not much is known about the CO_2 cloud microphysics and especially about the CO_2 snow metamorphism on the ground, we have chosen not to distinguish these two cases. In fact, both the surface snow (by reducing the surface emissivity) and the clouds (by backscattering the infrared radiation) decrease the net infrared radiative fluxes at the surface and at the top of the atmosphere. For the ground, and for the "space" above the atmosphere, the radiative balance is the same with both processes. In the model, we shall therefore simply reduce the

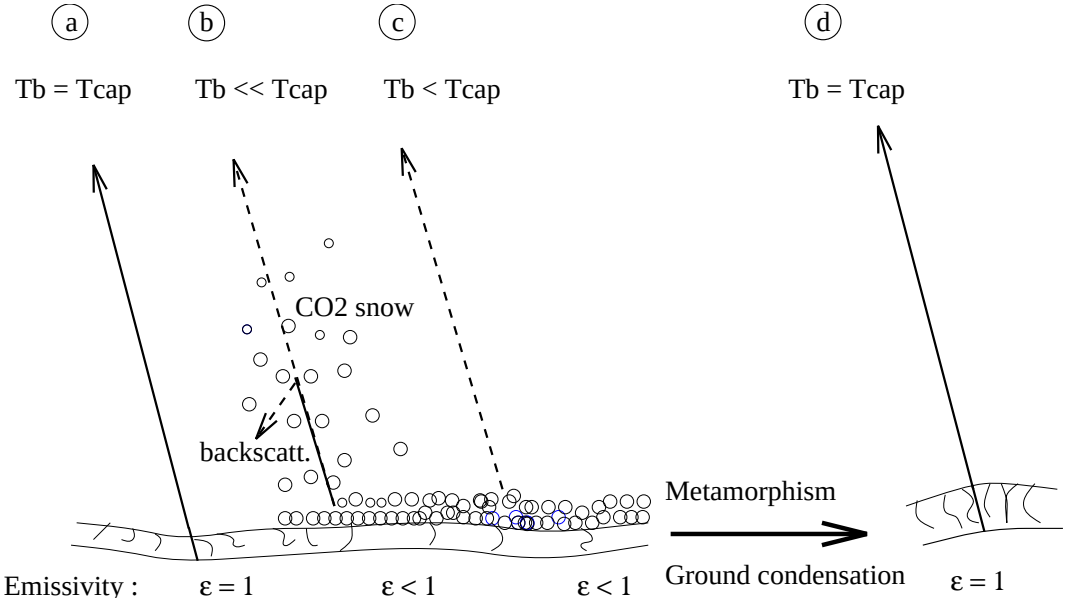

Figure 12: Schematic representation of the CO_2 snow fall scenario parametrized in the model to simulate the "low emission zones" observed in the polar night (see *Forget et al.*, 1995, 1996). (a) outside of the low emission zones, the cap emissivity ϵ is close to one; (b) During a snow fall, the airborne CO_2 ice particles scatter the thermal radiation back to the ground, and, once on the ground decrease the surface emissivity ϵ; (c) After the end of the snow fall, the emissivity ϵ remains below one until metamorphism and ground condensation increase the CO_2 ice grain size, and thus ϵ; (d) Ultimately, the ice layer become nonporous and transparent, and the infrared radiation emitted by the ground can radiate through with $\epsilon \simeq 1$

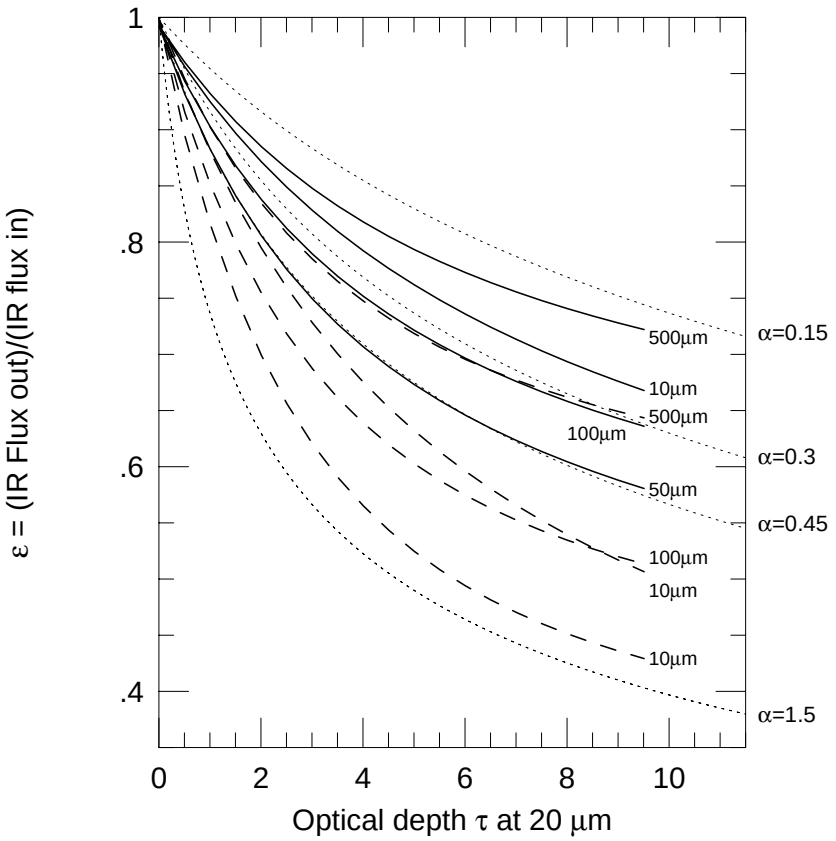

Figure 13: Decrease of the infrared flux radiated toward space due to CO_2 ice particles of radius 10, 50, 100 et 500 μm. The particles and surface temperature is 145 K. The CO_2 ice is pure (dashed lines) or mixed with 10 g.m^{-2} of water ice (solid lines). The dotted lines show examples of the curve $\varepsilon = (1 + \alpha\tau)^{-1/3}$.

surface emissivity. The main impact of such a simplification is to underestimate the infrared flux between the surface and the top of the scattering clouds. In fact, the model predicts that most of the atmospheric condensation occurs near the ground. Moreover, only the precipitating clouds, with particle sizes larger than 10 μm (and thus close to the ground) are able to efficiently scatter the thermal radiation.

6.2 Variation of the snow emissivity

The emissivity ε of the system [ground + ice + fresh snow + clouds] decreases with the accumulation of particles having condensed in the atmosphere. This decrease is limited by the condensation on the ground and more generally by some snow metamorphism processes (Eluszkiewicz, 1993).

Decrease of ε: At any moment, the atmospheric condensation accumulate a layer of mass m (kg.m^{-2}) of scattering particles. The particles size in this layer is probably extremely variable, from the top of the clouds to the snow layers underneath. For our parametrization, a detailed knowledge of the vertical distribution of the particle sizes is not necessary since we are only concerned by the global impact of the entire layer on the radiation budget. Thus, we can assume that this layer is composed of particles with an equivalent radius r. This radius probably ranges

between 10 μm (the minimum size to efficiently scatter the thermal radiations) and a few hundreds micrometers.

At a given wavelength (20 μm), The scattering particles layer optical depth is given by:

$$\tau = \frac{3Q_{ext}}{4\rho r} m \tag{70}$$

Where ρ is the CO_2 ice density (1630 kg m^{-3} at 140 K), Q_{ext} the extinction parameter at 20 μm, here close to the scattering parameter Q_{scat}. According to the Mie theory, Q_{ext} should be close to its asymptotic value 2 for the particles larger than 25 μm. For the particles with radius between 10 and 25 μm, Q_{ext} could theoretically reach 4 because of resonancy processes. In reality, however, the broad size distribution around r should decrease these effects (Hansen and Travis, 1974) and we should have $Q_{ext} \simeq 2$. The optical depth τ should thus only be function of r and m: $\tau \simeq 10^{-3}\, m/r$.

The impact of such a layer of optical depth τ on the thermal radiation can be computed with a radiative transfer model (See Forget et al., 1995). The results, presented on figure 13, show that the decrease of the infrared flux depends upon the particule radius and the amount of water ice mixed with the CO_2 ice (such water ice particles are thought to be present at least in the northern hemisphere). The Y-axis in figure 13 corresponds to the emissivity ε of the system ground + scattering layer that we are parametrizing. In most realistic cases, ε is well approximated by $\varepsilon = (1 + \alpha\tau)^{-1/3}$ with $0.15 < \alpha < 1.5$, $\alpha = 0.45$ being an appropriate mean value.

We can thus write:

$$\varepsilon = (1 + 10^{-3}\, \frac{\alpha}{r} m)^{-1/3} \tag{71}$$

A time derivation gives the equation governing the decrease of ε:

$$\frac{\partial \varepsilon}{\partial t} = -\frac{10^{-3}}{3}\, \varepsilon^4\, \frac{\alpha}{r} \frac{\partial m}{\partial t} \tag{72}$$

$\partial m/\partial t$ corresponds to the atmospheric condensation rate (kg.m^{-2}.s^{-1}).

Increase of ε : In theory, many factors are likely to influence the increase of the snow emissivity due to the growth of the CO_2 grains: direct condensation on the ground, sublimation, etc... However, no observations are available. To simplify, we have assumed that ε was restored toward unity with a timescale $\mathcal{T}$:

$$\frac{\partial \varepsilon}{\partial t} = \frac{1}{\mathcal{T}}(1 - \varepsilon) \tag{73}$$

$\mathcal{T}$ should be of the order of the low emission zones time scale observed by Viking: about one day.

Evolution of ε : The governing equation for the emissivity ε as a function of the condensation rate $\partial m/\partial t$ is:

$$\frac{\partial \varepsilon}{\partial t} = -\frac{10^{-3}}{3}\, \varepsilon^4\, \frac{\alpha}{r} \frac{\partial m}{\partial t} + \frac{1}{\mathcal{T}}(1 - \varepsilon) \tag{74}$$

This scheme only depends on two "unknown" parameters $\mathcal{T}$ and r (actually α/r, but α is set to its mean value $\alpha = 0.45$, r remaining variable). Besides, the stationary solution of equation 74 (corresponding to $\frac{\partial \varepsilon}{\partial t} = 0$) only involved the ratio $r/\mathcal{T}$. On average, this ratio will control the value of ε.

6.3 Numerical scheme

At every timestep, $\delta\varepsilon$ is added to ε ($\varepsilon_{t+\delta t} = \varepsilon_t + \delta\varepsilon$). The atmospheric condensation rate is calculated by the model in every layer: $\frac{\partial m}{\partial t} = \sum_{k=1}^{N} \frac{\delta m_k}{\delta t}$ (with the notation of the previous section). In the GCM, the physical parametrizations timestep is of the order of 1/40 day. The equation 74 cannot be approximated directly by $\delta\varepsilon/\delta t = \partial\varepsilon/\partial t$ because δt may be too long compared to the time constant of the term from equation 73 (Typically $[\frac{10^{-3}}{3}\,\varepsilon^3\,\frac{\alpha}{r}\sum_{k=1}^{N}\frac{\delta m_k}{\delta t}]^{-1}$). Nevertheless, if we assume that the increasing and the decreasing terms can be separated ($\delta\varepsilon = \delta\varepsilon_\uparrow + \delta\varepsilon_\downarrow$), $\delta\varepsilon_\downarrow$ can be derived from the integration of équation 72 over one timestep:

$$\varepsilon^{-3} - (\varepsilon + \delta\varepsilon_\downarrow)^{-3} = -10^{-3}\,\frac{\alpha}{r}\sum_{k=1}^{N}\frac{\delta m_k}{\delta t} \tag{75}$$

The increasing term, on the other hand, can directly be computed from equation 73 with $\frac{\delta\varepsilon_\uparrow}{\delta t} = \frac{1}{\mathcal{T}}(1-\varepsilon)$, since we should always have $\delta t << \mathcal{T}$.

At every timestep, the increment is thus given by [2] :

$$\delta\varepsilon = (\varepsilon^{-3} + 10^{-3}\,\frac{\alpha}{r}\sum_{k=1}^{N}\delta m_k)^{-1/3} - \varepsilon + \frac{\delta t}{\mathcal{T}}(1-\varepsilon) \tag{76}$$

6.4 Computational aspect

The CO_2 snow scheme subroutine `co2snow` is called by condensation sublimation scheme `newcondens`:

```
      SUBROUTINE co2snow (ngrid,nlayer,ptimestep,emisref,condsub,pplev,
     &        paerosol,pcondicea,pcondices,pfallice,pemisurf,
     &             pdaerosol)

       IMPLICIT NONE

c=======================================================================
c     Program for simulate the impact of the CO2 snow fall on
c     the surface infrared emission (emissivity)  and on
c     the airborne dust
c     F.Forget 1996
c=======================================================================

c   input:
c   ------
c    ngrid                number of grid point in the horizontal physical grid
c    nlayer               number of layers
```

[2] In practice, the emissivity ε_0 of the ground below the ice is lower than unity ($\varepsilon_0 = 0.95$ in the model). The actual polar cap emissivity in the model ε_m is thus given by the product $\varepsilon \times \varepsilon_0$ with ε computed following equation 74. Its governing equation is thus:

$$\frac{\partial\varepsilon_m}{\partial t} = -\frac{10^{-3}}{3}\,\frac{\varepsilon_m^4}{\varepsilon_0^3}\,\frac{\alpha}{r}\frac{\partial m}{\partial t} + \frac{1}{\mathcal{T}}(\varepsilon_0 - \varepsilon_m)$$

In the model, we shall use the integrated version:

$$\delta\varepsilon_m = [(\frac{\varepsilon_m}{\varepsilon_0})^{-3} + 10^{-3}\,\frac{\alpha}{r}\sum_{k=1}^{N}\delta m_k]^{-1/3} - \varepsilon_m + \frac{\delta t}{\mathcal{T}}(\varepsilon_0 - \varepsilon_m)$$

```
c    ptimestep             physical timestep (s)
c    condsub(ngrid)        logical : cond. or sub. at this grid point ?
c    pplev(ngrid,nlayer+1) Pressure levels (interface)
c    paerosol(ngrid,nlayer) Dust optical depth in each box
c    pcondicea(ngrid,nlayer)Atmospheric condensation rate (kg.m-2.s-1)
c    pcondices(ngrid)       Surface  condensation rate (kg.m-2.s-1)
c    pfallice(ngrid,nlayer) falling ice (kg.m-2.s-1)
c
c   Input / output
c   --------------
    emisref(ngrid) emissivity of ``the ground below the ice''
    pemisurf(ngrid) surface emissivity
    pdaerosol(ngrid,nlayer) not used in the ESA project


c Implicit argument
c -----------------

#include "dimensions.h"
#include "dimphys.h"
#include "comcstfi.h"
#include "surfdat.h"
```

7 Choice of the vertical discretization

One important improvement of the GCM for the contract is the use of a refined grid. The choice of the horizontal grid is rather straightforward. The fields are interpolated on a Gaussin grid in the Oxford spectral version and the LMD grid point version uses equally spaced points in latitude and longitude.

The choice of the vertical grid is more difficult since we want to have both a fine resolution near the surface corresponding to the environment of a landing probe as well as a large vertical extension reaching an effective height of about 80 km.

This was acheived by using the following analytical function for the σ-levels (the vertical coordinate σ of the model is the pressure normalized by its surface value)

$$\sigma_l = \frac{1.}{1. + C\left[\exp E(l-1) - 1\right]} \tanh\left[\frac{.5 * (N + 1 - l)}{NH}\right] \tag{77}$$

where N is the total number of layers.

The first term on the right hand side is close to a geometric progression near the surface (the ration between the thickness of two consecutive layers is about constant) and results in constant layer thickness (in meters) in the rest of the atmosphere. The tanh term is introduced in order to have a slow transition to a zero pressure over the NH upper layers of the model.

E and C constants are computed from the thickness of the first layer and from the total atmospheric vertical extension.

Table 1 gives the distribution of the 25 layers for a first layer 10 m thick, an effective vertical coverage of 80 km and 2 layers for the transition zone at the top, which was chosen for the database simulations.

N	σ-levels		Altitudes (m)		
	Mid layer	Top	Mid Layer	Top	Thickness
1	0.9996	0.9990	3.6	10.0	10.0
2	0.9984	0.9972	16.4	28.1	18.1
3	0.9960	0.9939	39.8	60.9	32.8
4	0.9918	0.9880	82.1	120.5	59.6
5	0.9842	0.9774	159.0	228.1	107.6
6	0.9707	0.9587	297.9	421.3	193.2
7	0.9468	0.9264	547.0	764.1	342.8
8	0.9059	0.8728	988.4	1360.2	596.1
9	0.8392	0.7895	1753.3	2363.3	1003.0
10	0.7386	0.6725	3030.1	3967.7	1604.5
11	0.6042	0.5293	5037.8	6361.4	2393.6
12	0.4523	0.3812	7934.2	9644.6	3283.2
13	0.3101	0.2522	11708.6	13775.8	4131.3
14	0.1979	0.1557	16197.5	18598.4	4822.5
15	0.1201	0.9144×10^{-1}	21192.6	23921.1	5322.7
16	0.7050×10^{-1}	0.5189×10^{-1}	26522.0	29585.4	5664.3
17	0.4045×10^{-1}	0.2875×10^{-1}	32076.2	35491.2	5905.7
18	0.2282×10^{-1}	0.1561×10^{-1}	37802.0	41597.3	6106.1
19	0.1265×10^{-1}	0.8297×10^{-2}	43698.9	47918.4	6321.1
20	0.6870×10^{-2}	0.4284×10^{-2}	49805.5	54529.5	6611.1
21	0.3609×10^{-2}	0.2115×10^{-2}	56242.3	61588.5	7058.9
22	0.1808×10^{-2}	0.9687×10^{-3}	63156.2	69395.2	7806.7
23	0.8212×10^{-3}	0.3869×10^{-3}	71047.8	78572.4	9177.2
24	0.3282×10^{-3}	0.1125×10^{-3}	80217.5	90921.3	12348.9
25	0.6535×10^{-4}	0	96358.2	–	–

Table 1: Vertical resolution of the GCM chosen for the database simulations.

References

P. G. Baines and T. N. Palmer. Rationale for a new physically-based parametrisation of sub-grid scale orographic effects. Technical Report 169, Eur. Cent. for Medium-Range Weather Forecasts, Reading, England, 1990.

A. K. Blackadar. The vertical distribution of wind and turbulent exchange in neutral atmosphere. *J. Geophys. Res.*, 67:3095–3102, 1962.

R. T. Clancy, S. W. Lee, G. R. Gladstone, W. W. McMillan, and T. Rousch. A new model for Mars atmospheric dust based upon analysis of ultraviolet through infrared observations from Mariner 9, Viking, and Phobos. *J. Geophys. Res.*, 100: 5251–5263, 1995.

D. S. Colburn, J. B. Pollack, and R. M. Haberle. Diurnal variations in optical depth at Mars. *Icarus*, 79:159–189, 1989.

Janusz Eluszkiewicz. On the microphysical state of the Martian seasonal caps. *Icarus*, 103:43–48, 1993.

F. Forget and J.B. Pollack. Thermal infrared observations of the condensing Martian polar caps: CO_2 ice temperatures and radiative budget. *J. Geophys. Res.*, 101: 16,865–16,880, 1996.

F. Forget, J. B. Pollack, and G. B. Hansen. Low brightness temperatures of Martian polar caps: CO_2 clouds or low surface emissivity? *J. Geophys. Res.*, 100:21,119–21,234, 1995.

Y Fouquart and B. Bonnel. Computations of solar heating of the Earth's atmosphere: A new parametrization. *Contrib. Atmos. Phys.*, 53:35–62, 1980.

B. A. Galperin, L. H. Kantha, S. Hassid, and A. Rosati. A quasi-equilibrium turbulent energy model for geophysical flows. *J. Atmos. Sci.*, 45:55–62, 1988.

James E. Hansen and Larry D. Travis. Light scaterring in planetary atmosphere. *Space Sci. Rev.*, 16:527–610, 1974.

H. M. Helfand and J. C. Labraga. Design of a nonsingular level 2.5 second-order closure for the prediction of atmospheric turbulence. *J. Atmos. Sci.*, 45:113–132, 1988.

F. Hourdin, Phu Le Van, F. Forget, and O. Talagrand. Meteorological variability and the annual surface pressure cycle on Mars. *J. Atmos. Sci.*, 50:3625–3640, 1993.

F. Hourdin, F. Forget, and O. Talagrand. The sensitivity of the Martian surface pressure to various parameters: A comparison between numerical simulations and Viking observations. *J. Geophys. Res.*, 100:5501–5523, 1995.

Frédéric Hourdin. A new representation of the CO_2 15 μm band for a Martian general circulation model. *J. Geophys. Res.*, 97(E11):18,319–18,335, 1992.

Hugh H. Kieffer, T. Z. Martin, R. Peterfreund, Bruce M. Jakosky, Ellis D. Miner, and Frank Don Palluconi. Thermal and albedo mapping during the Viking primary mission. *J. Geophys. Res.*, 82:4249–4291, 1977.

R. S. Lindzen. Turbulence and stress owing to gravity wave and tidal breakdown. *J. Geophys. Res.*, 86:9707–9714, 1981.

Terry Z. Martin. Thermal infrared opacity of the Mars atmosphere. *Icarus*, 66: 2–21, 1986.

George L. Mellor and Tetsuji Yamada. Development of a turbulence closure model for geophysical fluid problems. *Rev. of Geophys.*, 20(4):851–875, November 1982.

M. J. Miller, P. M. Palmer, and R. Swinbank. Parametrisation and influence of sub-grid scale orography in general circulation and numerical weather prediction models. *Meteorol. Atmos. Phys.*, 40:84–109, 1989.

J. F. Mustard and J. F. Bell III. New composite reflectance spectra of Mars from 0.4 to 3.14 μm. *Geophys. Res. Lett.*, 21:353–356, 1994.

M.E. Ockert-Bell, J. B. Pollack, and J.F. Bell. Wavelength dependance of the radiative properties of Martian atmospheric dust. *Bull. Am. Astron. Soc.*, 26: 1130, 1994.

T. N. Palmer, G. J. Shutts, and R. Swinbank. Alleviation of a systematic westerly bias in general circulation and numerical weather prediction models through an orographic gravity wave drag parametrisation. *Q. J. R. Meteorol. Soc.*, 112: 1001–1039, 1986.

S. P. Phillips. Analytical surface pressure and drag for linear hydrostatic flow over three-dimensional elliptical mountains. *J. Atmos. Sci.*, 41:1073–1084, 1984.

T. Roush, J. B. Pollack, and J. Orenberg. Derivation of midinfrared (5-25 μm) optical constants of some silicates and palagonite. *Icarus*, 94:191–208, 1991.

O. B. Toon, J. B. Pollack, and C. Sagan. Physical properties of the particles composing the Martian dust storm of 1971-1972. *Icarus*, 30:663–696, 1977.

O. B. Toon, C. P. McKay, T. P. Ackerman, and K. Santhanam. Rapid calculation of radiative heating rates and photodissociation rates in inhomogeneous multiple scattering atmospheres. *J. Geophys. Res.*, 94:16,287–16,301, 1989.

E.W. Washburn. *International critical tables of numerical data,physics, chemistry, and technology, volume 3.* New York: McGraw Hill, 1948.

S. E. Wood, M. I. Richardson, and D. A. Paige. Microphysical and radiative processes in CO_2 snow on Mars. Oral presentation at the 27th annual DPS meeting (Kona). Abstracts book, p44, 1995.

S. S. C. Wu. A method of defining topographic datums of planetary bodies. *Annales de Geophysique*, 1:147–160, 1981.